

# Generation of a Passive, Underdense Plasma Lens for the Focusing of Relativistic Electron Beams

by

Matthew Guerrero

Prof. Michael Litos, Thesis Advisor, Physics Department

Prof. Paul Beale, Honors Council Representative, Physics Department

Prof. Erica Nelson, Outside Reader, Astrophysical and Planetary Sciences Department

A thesis submitted in partial fulfillment

of the requirements for the

Degree of Bachelor of Arts in Physics

University of Colorado Boulder

April 2, 2024

# Abstract

The viability of a plasma wakefield accelerator is limited by the projected emittance growth of an accelerated electron beam due to chromatic phase spreading. This can be mitigated through beam-matching via use of a plasma lens, which offers greatly-increased performance when compared to conventional quadrupole magnetic focusing. We conducted experiments using a proposed cylindrical-lens telescope with multiple laser systems, and found that installation and alignment of this lens system is possible without high-precision components. A properly-sized incident laser beam, focused through these lenses, reaches the optimal dimensions to ionize a plasma lens for use in a plasma wakefield accelerator. We measured the best focus to have a minor axis of  $34.5 \pm 3.45 \mu\text{m}$  and a major axis of  $120.75 \pm 3.45 \mu\text{m}$ , which compares favorably with the predicted minor axis of  $37.4 \mu\text{m}$  and major axis of  $118.5 \mu\text{m}$ .

# Acknowledgments

I would like to extend my deepest gratitude to my advisor, Dr. Mike Litos, for his mentorship, guidance, and depth of knowledge throughout the two years I spent in his lab. I would also like to thank all of the graduate students in the CU Wakefield Acceleration and Radiation Generation research group (CU-WARG) for their patience and for all the help they provided for me over the course of this project. I would especially like to thank my research partner Leah Hartman of Western Kentucky University, without whose support, both in and out of the lab, I would never have completed my thesis.

I would also like to thank Ángel Hernandez, Abby Hartley, Maeve Rodgers, and countless other friends and colleagues I do not have the room to list here, for motivating me to persist through my studies and expand my horizons as a scientist.

I want to thank my mother, father, and sister for their continued encouragement.

And finally, I would like to thank Tianna Juárez, who has been my greatest supporter through this process.

This material is based upon work supported by the U.S. Department of Energy, Office of Science, Office of High-Energy Physics, under Award Number DE-SC001796 and by the National Science Foundation under Grant Number PHY-2047083.

# Contents

<b>Abstract</b>	<b>i</b>
<b>Acknowledgments</b>	<b>ii</b>
<b>1 Introduction</b>	<b>1</b>
1.1 Background . . . . .	1
1.2 Beam Focusing . . . . .	2
<b>2 Plasma Formation and PWFA</b>	<b>3</b>
2.1 Laser Ionization . . . . .	3
2.2 Plasma Acceleration . . . . .	5
2.2.1 Plasma Wakefield Acceleration in the Nonlinear Blowout Regime . . .	7
<b>3 Plasma Lens</b>	<b>9</b>
3.1 Plasma Wakefield Dynamics . . . . .	9
3.1.1 Betatron Motion . . . . .	13
3.2 The Plasma Lens . . . . .	13
<b>4 Laboratory Optics</b>	<b>16</b>
4.1 Ultrashort Laser Pulses . . . . .	16
4.1.1 Bandwidth Analysis of Ultrashort Lasers . . . . .	16
4.1.2 Chirped-Pulse Amplification . . . . .	17
4.2 Laser System . . . . .	18
4.2.1 Wavefront Optimization . . . . .	19
4.3 Gaussian Optics . . . . .	21
4.3.1 Cylindrical Lenses . . . . .	23
<b>5 Visible Laser Experimental Tests</b>	<b>24</b>
5.1 Two-Lens Experimental Design . . . . .	24
5.1.1 Experimental Considerations . . . . .	26
5.1.2 Data Collection Procedure . . . . .	26
5.1.3 Results . . . . .	27
5.2 Three-Lens Experimental Design . . . . .	29

5.2.1	Data Collection . . . . .	30
5.2.2	Results . . . . .	30
<b>6</b>	<b>Infrared Laser Experimental Tests</b>	<b>32</b>
6.1	IR Laser Diode Tests . . . . .	32
6.1.1	Experimental Design . . . . .	32
6.1.2	Results . . . . .	33
6.2	Centaurus Laser Tests . . . . .	36
6.2.1	Experimental Design . . . . .	36
6.2.2	Results . . . . .	37
<b>7</b>	<b>Conclusions and Future Work</b>	<b>40</b>
7.1	Future Work . . . . .	40
7.1.1	At CU-WARG Laboratory . . . . .	40
7.1.2	At SLAC . . . . .	41
7.2	Conclusions . . . . .	42

# List of Figures

1.1	Field diagram of a quadrupole focusing magnet. [20]	2
2.1	Strong-field ionization regimes: (a) Tunneling ionization; (b) Barrier-suppression ionization. [23]	5
2.2	Post-breakdown cratering of a copper RF cavity [26].	6
2.3	Particle-in-Cell (PIC) Simulation of a relativistic electron beam accelerated in a plasma blowout wake formed by a relativistic drive beam.	7
3.1	Planar cross-sections of plasma lens profile, with electron beam trajectory marked in cyan and laser trajectory marked in red. Clockwise from left: $y - z$ plane (side view), $x - y$ plane (front view), $x - z$ plane (top view).	14
4.1	Schematic of WARG Lab Centaurus Laser System	18
4.2	Photographs of CU-WARG Centaurus Laser system	19
4.3	Detail of Experimental Chamber A, containing deformable mirror for wavefront-correction.	19
4.4	Cross-section of deformable mirror displaying piston control of mirror surface.	20
4.5	Evolution of a Gaussian beam near the beam waist. [40]	22
4.6	Schematic and photos of cylindrical lenses. The ability to focus along a single transverse axis is integral to the lens design presented here.	23
5.1	Intensity profile of HeNe laser before (left) and after (right) spatial filtering.	24
5.2	Schematic of two-lens experimental setup.	25
5.3	Overhead photo of two-lens experimental setup.	25
5.4	Ray-trace diagram for a converging lens with no ND filter (left) and with an ND filter (right). The dashed line denotes the nominal focal plane.	26
5.5	Coarse scan of the evolution of laser beam waist near the focal plane of individual lenses. Each dataset consists of 21 images collected with a 1 mm step size.	27
5.6	Fine scan of the evolution of laser beam waist near the focal plane of individual lenses. Each dataset consists of 41 images collected over a 2mm range with a 50 $\mu\text{m}$ step size.	28

5.7	Scans of the evolution of laser beam waist near the focal plane of the orthogonally combined +200 mm and +700 mm lenses. Coarse scan (left) consists of 21 data points collected over a 3mm range in $30\mu\text{m}$ steps. Fine scan (right) consists of 41 data points collected over a 1.6mm range in $40\mu\text{m}$ steps. . . .	28
5.8	Schematic of three-lens experimental setup. . . . .	29
5.9	Overhead photo of three-lens experimental setup. . . . .	30
5.10	Fine scan of the evolution of minor axis of the laser beam waist near the focal plane of the lenses using the 520 nm laser. . . . .	31
5.11	Intensity profile of the 520 nm laser at the focus of the three-lens setup. . . .	31
6.1	IR diode laser experimental setup. . . . .	33
6.2	Diode laser post-expander. This beam diameter, $6\text{ mm} \pm 1\text{ mm}$ , corresponds to an expected final beam waist of $61.1 \pm 10\mu\text{m}$ and a Rayleigh length of $15 \pm 5\text{ mm}$ . . . . .	34
6.3	Scan of the evolution of minor axis of the laser beam waist near the focal plane of the lenses using the IR diode laser. . . . .	35
6.4	Intensity profile of the IR diode laser at the focus of the three-lens setup. . .	35
6.5	Pulsed IR laser experimental setup. . . . .	36
6.6	Intensity profile of the pulsed IR laser at points equidistant from the focal point, $z(w_0)$ . Note that diffraction effects shift to opposite sides of the center as the beam progresses through the waist, likely due to a tilt of the vertically focusing lens. . . . .	38
6.7	Scan of the evolution of minor axis of the laser beam waist near the focal plane of the lenses using the pulsed IR laser. . . . .	38
6.8	Intensity profile of the pulsed IR laser at the focus of the three-lens setup. . .	39
7.1	Schematic of the reflective beam-reducer telescope. Beam is incident from the right side of the figure. . . . .	41
7.2	SLAC experimental vacuum chamber installed along the electron beam line. Gas from a gas jet is ionized by a laser pulse to form a plasma lens, which then focuses the relativistic electron beam. [28] . . . . .	42

# List of Tables

3.1	Comparison between focusing elements of a 10 GeV electron beam [28], normalized such that $\sqrt{K} \times L$ is equivalent for each optic. . . . .	15
6.1	Laser intensity at 10 mJ pulse energy, assuming an initial beam radius of 5mm.	37

# Chapter 1

## Introduction

### 1.1 Background

Particle accelerators have been vital to the scientific community ever since their invention in the early twentieth century. They allow physicists to search ever deeper into the constituent parts of matter, and provide insight to the creation of the universe which we all inhabit. Particles accelerated by the Large Hadron Collider (LHC) in Geneva have a final energy of 6.5 TeV and thus a total collision energy of 13 TeV. Accelerated particles are also used in radiation therapy for cancer treatment and electron beam microscopy, and are considered as a candidate for precision cutting and welding in industrial manufacturing. [1]

A number of landmark scientific discoveries were only made possible due to the precision and reliability of existing particle accelerators [2–9], significantly increasing our knowledge of matter. In the more distant long-term, higher-energy accelerators can allow us to derive insight into even smaller subatomic scales than we are able to currently. Accelerator structures are also vital for a number of medical and industrial uses, such as particle beam probing for sample analysis in physics, biology, and chemistry [10–12], and can play central roles in public health and sanitization [13–17]. Accelerated particle beams have significant utility in their ability to modify the properties of matter through interaction, allowing the manufacture of everyday objects like shrink-wrap [18]. By reason of the centrality of particle accelerators to particle physics and a number of related scientific fields, as well as their ubiquity in the maintenance and advancement of modern everyday life, the continual improvement of existing accelerator technology, its miniaturization, and its progression into higher-energy frontiers is fundamental to the evolution of physics and society as a whole.

## 1.2 Beam Focusing

The utility of accelerated particles is limited by our ability to direct and control the charged particle beam. One metric for beam quality is *spot size*, or the transverse area of the accelerated beam [19]. This is generally controlled by the use of powerful quadrupole magnetic lenses. These are extremely useful, as they focus charged particles towards the longitudinal axis of acceleration. Furthermore, a magnetic field perpendicular to the trajectory of a moving charged particle does no work on the particle as a result of the Lorentz force law, and so any energy gained by the particle beam through acceleration is not lost through magnetic focusing.

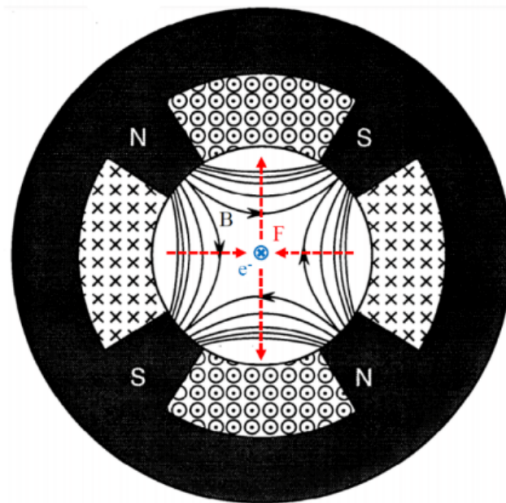


Figure 1.1: Field diagram of a quadrupole focusing magnet. [20]

The magnetic approach is robust, but not without drawbacks. As the quadrupole magnet focuses the particle beam along a single transverse axis, the magnetic field also causes other parts of the beam to diverge along the other transverse axis. This effectively defocuses the beam, as displayed by the red force vectors in Figure 1.1. Accelerator facilities mitigate this by using several quadrupole magnet assemblies, rotated  $90^\circ$  relative to each other. This technique is highly expensive, requires lots of space, and provides multiple potential points of failure. Though the primary goal of this project is immediately suited to emittance preservation in a plasma wakefield accelerator (see Section 2.2) it provides a powerful method to mitigate the disadvantages of quadrupole magnetic beam focusing.

# Chapter 2

## Plasma Formation and PWFA

### 2.1 Laser Ionization

Plasma is formed when electrons bound to the nuclei of gas atoms are stripped away to travel freely. This can occur several ways. If the gas is heated, the average kinetic energy of the gas molecules increases. If two atoms or an atom and electron collide with enough force, it is possible for the impact to impart enough energy into a valence electron, knocking it free from the Coulomb potential of the nucleus. This process is called *thermal ionization*.

It is also possible to ionize a plasma using intense light, since photons also carry energy. If an electron is bombarded by enough energetic photons, it can overcome the binding energy of the nucleus. This does pose some practical issues, however. The quickest, and most repeatable, method for ionization in this way is to use a laser. We can determine the wavelength of a photon energetic enough to overcome the hydrogen ground-state energy of 13.6 eV:

$$E = \frac{2\pi\hbar c}{\lambda} \implies \lambda = \frac{2\pi\hbar c}{E} \quad (2.1)$$

For a photon to carry energy  $E = 13.6$  eV, we find that its wavelength must be around 90 nm, placing it in the ultra-violet regime. Most laboratory laser systems have longer wavelengths than this, requiring multiple photons to interact with the electron in order to ionize it.

The most economical ionization technique makes use of a laser. Rather than employing a laser as a vehicle for energetic photons, however, it makes use of the intense electric field constituting the laser pulse to generate a plasma. An electron bound to a nucleus sits within a funnel defined by the Coulombic potential of the nucleus, given as

$$\Phi = \frac{q_e}{4\pi\epsilon_0 r} \quad (2.2)$$

A high-power laser is applied to a neutral gas. This causes the potential funnel to “tilt,” decreasing the maximum energy required for the electron to escape. As the potential funnel

is suppressed, there exists a point where the electron's ground-state energy is greater than the Coulomb potential of the nucleus. The dashed line in Figure 2.1 becomes steeper as the energy carried by the laser pulse (and thus laser intensity) increases. Eventually, the potential funnel can be suppressed so thoroughly that even the ground state energy of the electron  $E_1$  is greater than the Coulomb potential, allowing the electron to freely leave the nucleus. This is said to be within the *barrier-suppression regime*. The intensity threshold for a laser to ionize atoms through barrier-suppression is on the order of  $10^{16} \text{ W/cm}^2$ .

A laser intense enough to fall within the barrier-suppression regime will guarantee ionization of plasma from a neutral gas. However, these lasers can have significantly high energy requirements, and require a large system of optical components in order to reach the required intensity. By making use of a fundamental principle of quantum mechanics, it is possible to laser-ionize a plasma with a smaller, cheaper, and much less-powerful laser.

The moment a laser is applied to a neutral gas, its electric field causes the Coulomb potential to no longer approach zero as  $r$  goes to infinity. Rather, it now defines a potential “bump” of finite width. As the laser intensity increases, the width, and maximal value, of the potential bump decreases. Due to the wavelike nature of quantum particles, there is a nonzero probability of measuring a particle within a classically-forbidden region, where its kinetic energy would have to be negative in order to satisfy  $E_{tot} = U + KE$ . The motion of these particles is dictated by the Schrödinger equation. For a one-dimensional system of total energy  $E$  characterized by a potential function  $V(x)$ , eigenfunctions of the Schrödinger equation are wavelike: [21]

$$\frac{\partial^2}{\partial x^2} \varphi_E(x) + \frac{2m(E - V(x))}{\hbar^2} \varphi_E(x) = 0 \quad (2.3)$$

Here  $\varphi_E(x)$  is an eigenfunction of the Schrödinger equation for a particle of mass  $m$ . Solutions to this are complex exponentials in classically-allowed regions, but are strictly real-valued exponentials where  $E < V(x)$ , and must approach zero to remain physically-viable as solutions. As a result of the continuity of wave functions, the probability of measuring a quantum particle “past” a potential boundary is directly correlated to the potential boundary's width. Broadly speaking, we can assert that, for a very narrow potential boundary, there is a high probability of measuring a particle past the boundary, though the details are of course a bit more complicated.

As the intensity of a laser incident on a neutral gas suppresses the Coulomb potential funnel, it eventually forces the width of the potential bump to be small enough that the electron has a very high probability of tunneling outside of the Coulomb potential well of the atom during the pulse length of the laser. This is the *tunneling-ionization regime*, as described in the Ammosov-Delone-Krainov (ADK) model for tunnel ionization. [22].

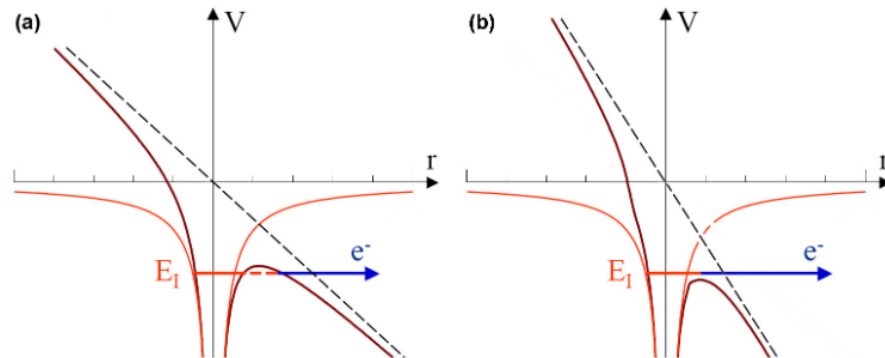


Figure 2.1: Strong-field ionization regimes: (a) Tunneling ionization; (b) Barrier-suppression ionization. [23]

It is important to note that, while the laser is applied, the neutral gas molecules are continuing to be bombarded by photons and multi-photon ionization continues to occur. For sufficiently-intense lasers, tunneling ionization becomes the dominant mode of ionization. The optimal laser intensity for laboratory plasmas, then, is one which allows electrons to ionize from their associated nuclei within the duration of the laser pulse, but not require more energy than is necessary. Tunneling ionization occupies a happy medium between multi-photon ionization and barrier suppression, and allows for repeatable laboratory plasma generation.

## 2.2 Plasma Acceleration

Accelerator structures can be miniaturized through the use of plasma. In conventional particle accelerators, a powerful electromagnetic wave propagates through a conductive waveguide called a *radio-frequency* (RF) cavity. The cavity is designed so that the phase velocity of the wave matches the velocity of the accelerating electrons, allowing the electrons to remain at a peak of the wave [24].

Though this is effective at accelerating particles, there is an upper limit to its strength. RF cavity-accelerators are made from copper, as it's a cheap, common, and relatively high-quality conductor. As the accelerating electric fields increase in strength, electrons can ionize from the walls of the cavity, leading to irreparable damage to accelerator structures [25].

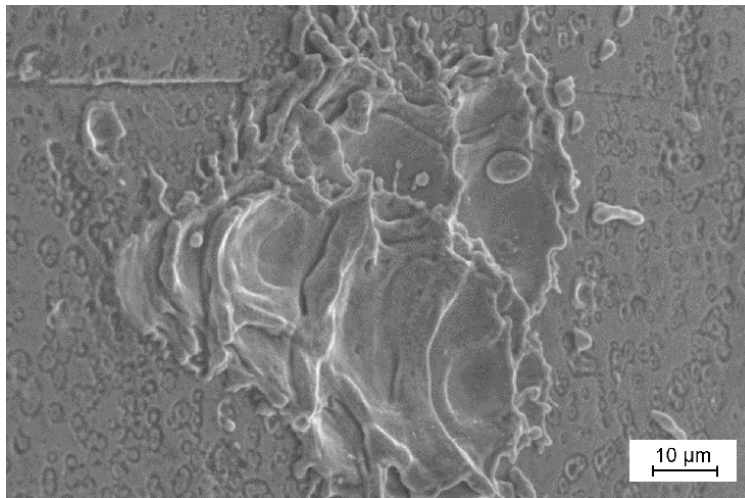


Figure 2.2: Post-breakdown cratering of a copper RF cavity [26].

RF-cavity breakdown imposes an upper limit on the strength of the accelerating field, leading to several practical limitations on buildable accelerators. Since operation within the high-gradient RF breakdown regime eventually degrades accelerator functionality beyond usability, higher energy thresholds can only be reached by increasing the size of conventional accelerator structures, rather than the accelerating field strength. As projected costs increase and usable space decreases, conventional accelerators seem to be reaching the extent of their capability to conduct experiments within new regimes. The maximum acceleration gradient, or energy gain per unit distance, achievable within an RF accelerator before cavity breakdown occurs is on the order of 100 MeV/m. Most conventional accelerators operate below this threshold. As new experiments call for increasing energy thresholds, accelerators get longer and longer to achieve the required final beam energy. The space required to build these, as well as the funds necessary, become prohibitively large to consider new conventional accelerator structures.

A novel technique to circumvent this was proposed in a paper by Tajima and Dawson in 1979, which makes use of a fundamental property of plasma to miniaturize accelerator structures and increase acceleration gradients [27]. A high-power laser ionizes a filament of plasma. This plasma is then perturbed by firing an intense, high-energy beam along its length. This can be either an intense, ultrashort (femtosecond) laser pulse, or a dense, high-energy electron bunch. This creates a cavitation inside of the plasma filament that propagates along with the beam. This is called the *plasma wake*, and the electromagnetic fields associated with it are the *plasma wakefields*. The plasma lensing technique proposed in Doss 2023 makes use of the latter [28].

### 2.2.1 Plasma Wakefield Acceleration in the Nonlinear Blowout Regime

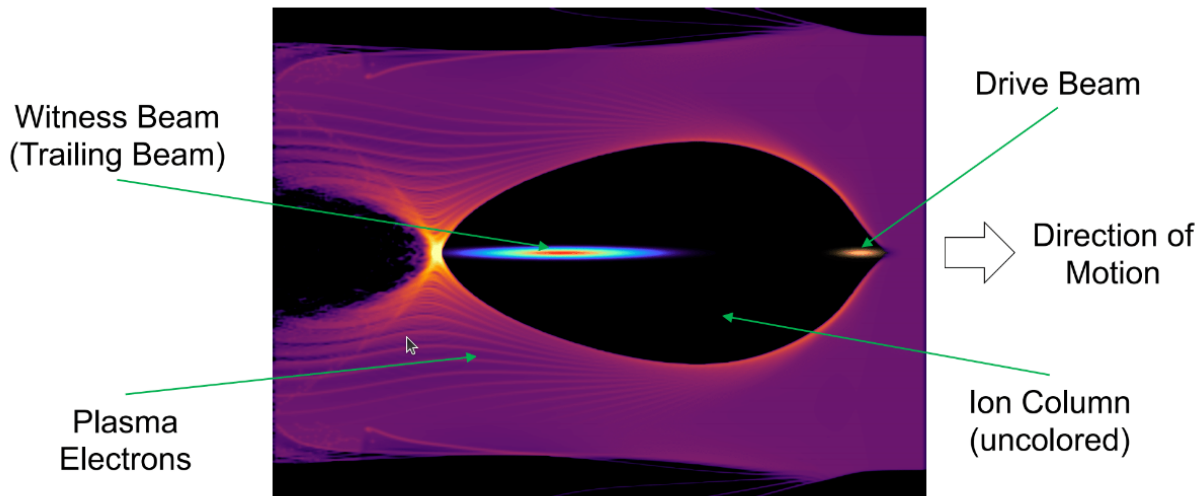


Figure 2.3: Particle-in-Cell (PIC) Simulation of a relativistic electron beam accelerated in a plasma blowout wake formed by a relativistic drive beam.

The method by which a plasma wake forms depends on the nature of the drive beam. When a relativistic electron bunch is used, its electric field pushes away plasma electrons. Special relativity dictates that, due to the speed of the electron bunch, the electric field is almost entirely in the radial direction, forcing the plasma electrons away from the axis of propagation. In the case of laser wakefield acceleration, plasma electrons experience a *ponderomotive force*, where the inhomogeneous oscillating electromagnetic field of the laser exerts a net force which, over one cycle, induces particle motion away from the region of highest field intensity. Both of these processes occur on timescales very fast compared to the average rate of ion motion, and a “bubble” of positively-charged ions called an *ion column* remains within the plasma. The ion column exerts a powerful transverse electric field, which pulls the plasma electrons displaced to form the wake back into the plasma filament.

As the electrons are knocked away, they form into a sheath at the leading edge of the wakefield column which has a greater electron density than the unperturbed plasma density. The plasma current in the electron sheath is responsible for the powerful accelerating force, which has been experimentally-verified to reach acceleration gradients of up to 160 GeV/m, over a thousand times more powerful than RF accelerators [29].

For point of comparison, the FACET-II RF accelerator cavities at SLAC National Laboratory have an average acceleration gradient of 20 MeV/m [30] resulting in an average energy

of 10 GeV. Further on, the beam-driven plasma accelerator provides an acceleration gradient of 10 GeV/m for a relativistic electron beam. One meter of plasma accelerator provides the same energy gain as one kilometer of conventional accelerator.

Though this technology shows significant potential for next-generation accelerators, it is not yet mature enough for wide-scale implementation. Plasma accelerators suffer from a lack of transverse emittance preservation, which can cause an irremediable increase in transverse beam spot size or instabilities resulting in total breakup of the electron beam [31]. This can be mitigated by “ramping” the density of the plasma filament and allowing the electron beam to “match” into the plasma [32, 33]. The electron beam needs to be focused to a precise spot size in order for this to work optimally.

This is not trivial to implement. Conventional electromagnets struggle to focus the relativistic electron beam to a size sufficiently-small enough to match into the density-ramped plasma. A plasma lens has a much stronger focus, and can effectively focus the electron beam to the necessary spot size. The plasma lens is thus an extremely potent tool for emittance preservation, and vitally-useful to the evolution of plasma wakefield accelerators.

# Chapter 3

## Plasma Lens

### 3.1 Plasma Wakefield Dynamics

Powerful electric fields within a nonlinear plasma wake are the driving force behind plasma wakefield acceleration. In a plasma lens, the extremely strong transverse electric fields are responsible for the radial force that leads to beam focusing. In order to examine exactly how this occurs, we can derive the transverse electric field strength inside a plasma wake.

Here we are restricting ourselves solely to a plasma within the nonlinear blowout regime. That is, we are considering the ion column formed by a relativistic electron beam fired through a quasineutral plasma filament. Over the timescale that this occurs, we can make several assumptions about what occurs within the wake, namely that the plasma ions remain stationary.

Two things result from this. First, since the plasma was ionized from a gas of uniform density, we will assume that the plasma is quasineutral, and that the ion density within the wakefield is simply the unperturbed ion density of the plasma  $n_i$ . The charge density within the column is then

$$\rho = en_i \tag{3.1}$$

We begin with the inhomogeneous wave equation forms of Gauss's Law and Ampere's Law in the Lorentz gauge. This is then

$$\left(\nabla^2 - \frac{1}{c^2} \frac{\partial^2}{\partial t^2}\right)\Phi = -\frac{\rho}{\epsilon_0} \tag{3.2}$$

$$\left(\nabla^2 - \frac{1}{c^2} \frac{\partial^2}{\partial t^2}\right)\mathbf{A} = -\mu_0\mathbf{J} \tag{3.3}$$

To satisfy the Lorentz gauge, we also have that

$$\nabla \cdot \mathbf{A} + \frac{1}{c^2} \frac{\partial \Phi}{\partial t} = 0 \tag{3.4}$$

We can split the above into transverse and longitudinal components:

$$\nabla_{\perp}^2 \Phi + \nabla_{\parallel}^2 \Phi - \frac{1}{c^2} \frac{\partial^2 \Phi}{\partial t^2} = -\frac{\rho}{\epsilon_0} \quad (3.5)$$

$$\nabla_{\perp}^2 \mathbf{A} + \nabla_{\parallel}^2 \mathbf{A} - \frac{1}{c^2} \frac{\partial^2 \mathbf{A}}{\partial t^2} = -\mu_0 \mathbf{J} \quad (3.6)$$

We can simplify this by transforming to a frame co-moving with the electron beam using the longitudinal coordinate  $\xi$ , where for some longitudinal position  $z$ ,

$$\xi = ct - z \quad (3.7)$$

In cylindrical coordinates, the longitudinal component of the Laplacian is simply the second derivative with respect to  $z$ . Using the substitution for  $\xi$ , this is then

$$\nabla_{\perp}^2 \Phi + \frac{\partial^2 \Phi}{\partial \xi^2} - \frac{1}{c^2} \left( c^2 \frac{\partial^2 \Phi}{\partial \xi^2} \right) = -\frac{\rho}{\epsilon_0} \quad (3.8)$$

$$\nabla_{\perp}^2 \mathbf{A} + \frac{\partial^2 \mathbf{A}}{\partial \xi^2} - \frac{1}{c^2} \left( c^2 \frac{\partial^2 \mathbf{A}}{\partial \xi^2} \right) = -\mu_0 \mathbf{J} \quad (3.9)$$

The derivatives with respect to  $\xi$  cancel, leaving only transverse components:

$$\nabla_{\perp}^2 \Phi = -\frac{\rho}{\epsilon_0} \quad (3.10)$$

$$\nabla_{\perp}^2 \mathbf{A} = -\mu_0 \mathbf{J} \quad (3.11)$$

We repeat the same process on the Lorentz gauge condition in cylindrical coordinates:

$$\begin{aligned} \nabla_{\perp} \cdot \mathbf{A}_{\perp} + \frac{\partial A_z}{\partial z} + \frac{1}{c^2} \left( \frac{\partial \Phi}{\partial \xi} \cdot \frac{\partial \xi}{\partial z} \right) &= 0 \\ \nabla_{\perp} \cdot \mathbf{A}_{\perp} - \frac{\partial A_z}{\partial \xi} + \frac{1}{c^2} \left( c \frac{\partial \Phi}{\partial \xi} \right) &= 0 \end{aligned} \quad (3.12)$$

Here we introduce the wakefield potential:

$$\psi \equiv \Phi - cA_z \quad (3.13)$$

We can rewrite the equation above in order to make a substitution:

$$\begin{aligned} \nabla_{\perp} \cdot \mathbf{A}_{\perp} &= \frac{\partial A_z}{\partial \xi} - \frac{1}{c} \frac{\partial \Phi}{\partial \xi} \\ &= -\frac{1}{c} \frac{\partial}{\partial \xi} (\Phi - A_z) \\ &= -\frac{1}{c} \frac{\partial \psi}{\partial \xi} \end{aligned} \quad (3.14)$$

We can also put the transverse Gauss's Law and Ampere's Law in terms of this wakefield potential by subtracting the longitudinal component of Eqn. 3.11 from Eqn. 3.10:

$$\begin{aligned}\nabla_{\perp}^2(\Phi - cA_z) &= -\frac{\rho}{\epsilon_0} + c\mu_0 J_z \\ \implies \nabla_{\perp}^2 \psi &= -\frac{1}{\epsilon_0}(\rho - c\mu_0 \epsilon_0 J_z) \\ &= -\frac{1}{\epsilon_0}\left(\rho - \frac{J_z}{c}\right)\end{aligned}\tag{3.15}$$

Using the cylindrical symmetry of the blowout wake, we can find relevant components of the scalar and vector potentials in terms of  $\xi$ : [28]

$$\begin{aligned}\Phi &= \Phi_0(\xi) - \frac{r^2}{4} \frac{en_0}{\epsilon_0} \\ A_z &= A_{z,0}(\xi) \\ A_r &= -r \frac{1}{2c} \frac{d\psi_0}{d\xi} \\ \psi &= \psi_0(\xi) - \frac{r^2}{4} \frac{en_0}{\epsilon_0}\end{aligned}\tag{3.16}$$

We also assume that the potential far from the wakefield blowout goes to zero. We then integrate over the blowout wake to determine the on-axis wakefield potential:

$$\psi_0 = \int_0^{\infty} \frac{1}{r} dr \int_0^r \frac{r'}{\epsilon_0} \left(\rho - \frac{J_z}{c}\right) dr'\tag{3.17}$$

In order to evaluate this, we assume that the electron sheath density is uniform, with width  $\Delta$ . The particular density profile follows from the continuity equation [28]:

$$\rho - \frac{J_z}{c} = -en_0 \frac{r_b^2}{(r_b + \Delta)^2 - r_b^2}\tag{3.18}$$

The on-axis wakefield potential integral then evaluates as

$$\psi_0(\xi) = \frac{en_0}{\epsilon_0} \frac{r_b^2(\xi)}{4} (1 + \beta(\xi))\tag{3.19}$$

Here the beta function  $\beta(\xi)$  is calculated from the wake potential, and depends on the properties of the electron sheath and the plasma ions [34, 35]. In the ultra-relativistic limit,  $\beta(\xi) \approx \frac{\Delta}{r_b}$  and  $\Delta \ll r_b$ , the wakefield potential simplifies to

$$\psi_0(\xi, r) = \frac{en_0}{4\epsilon_0} (r_b^2 - r^2)\tag{3.20}$$

Using this blowout potential, we are able to determine first the transverse electric field within the wake:

$$\begin{aligned}\mathbf{E} &= -\nabla\Phi - c\frac{\partial\mathbf{A}}{\partial t} \\ \mathbf{E}_\perp &= \left(-\frac{\partial\Phi}{\partial r} - c\frac{\partial\mathbf{A}_r}{\partial t}\right)\hat{r} + \left(-\frac{1}{r}\frac{\partial\Phi}{\partial\phi} - c\frac{\partial\mathbf{A}_\phi}{\partial t}\right)\hat{\phi} \\ &= \frac{r}{2}\left(\frac{en_0}{\epsilon_0} + \frac{d\psi_0}{d\xi}\right)\hat{r}\end{aligned}\quad (3.21)$$

We can also determine the transverse magnetic field:

$$\begin{aligned}\mathbf{B} &= \nabla \times \mathbf{A} \\ \Rightarrow \mathbf{B}_\perp &= \left(\frac{1}{r}\frac{\partial A_z}{\partial\phi} + \frac{\partial A_\phi}{\partial\xi}\right)\hat{r} - \left(\frac{\partial A_r}{\partial\xi} + \frac{\partial A_z}{\partial r}\right)\hat{\phi} \\ &= \frac{r}{2c}\frac{d\psi_0}{d\xi}\hat{\phi}\end{aligned}\quad (3.22)$$

The Lorentz Force Law gives an equation of motion for an electron within the plasma blowout:

$$\mathbf{F} = -e(\mathbf{E} + \mathbf{v} \times \mathbf{B}) = -e\mathbf{W} \quad (3.23)$$

Here we define a “wakefield” term  $\mathbf{W}$  to combine the contributions of both the electric and magnetic fields. With  $\mathbf{v} \approx c\hat{z}$ , the Lorentz Force Law gives the transverse wakefield terms:

$$\begin{aligned}\mathbf{W}_\perp &= \mathbf{E}_\perp + c\hat{z} \times \mathbf{B}_\perp \\ &= \frac{r}{2}\left(\frac{en_0}{\epsilon_0} + \frac{d\psi_0}{d\xi}\right)\hat{r} + \left(c\hat{z} \times \frac{r}{2c}\frac{d\psi_0}{d\xi}\hat{\phi}\right) \\ &= \frac{r}{2}\left(\frac{en_0}{\epsilon_0} + \frac{d\psi_0}{d\xi}\right)\hat{r} - \frac{r}{2}\frac{d\psi_0}{d\xi}\hat{r}\end{aligned}\quad (3.24)$$

The transverse magnetic field, generated solely by the plasma current, then cancels out with the  $\psi$ -dependent term of  $E_\perp$ , which leaves a single non-vanishing term:

$$\begin{aligned}\mathbf{W}_\perp &= \frac{1}{2}\frac{en_0}{\epsilon_0}r\hat{r} \\ &= \mathbf{E}_\perp\end{aligned}\quad (3.25)$$

This is the space-charge electric field of the ions within the blowout wake which is simply the transverse component of the electric field within the wake bubble.

### 3.1.1 Betatron Motion

If we consider a single electron within the wakefield bubble, we can determine its equation of motion using Newton's Second Law from Equation 3.25. We assume that the force of gravity on the electron is negligible compared to the Coulomb force from the wakefield. Then, since the transverse magnetic field within the wake is zero, we have that

$$\begin{aligned}
 m_e \frac{d^2 r}{dt^2} &= qE_{\perp} \\
 &= (-e) \left( \frac{1}{2} \frac{en_0}{\epsilon_0} r \right) \\
 \implies \frac{d^2 r}{dt^2} &= -\frac{e^2 n_0}{2\epsilon_0 m_e} r
 \end{aligned} \tag{3.26}$$

This describes a simple harmonic oscillator in the radial direction, which allows us to conclude that an electron accelerated within a PWFA will oscillate about the central axis as a result of the strong transverse Coulomb force present within the bubble.

## 3.2 The Plasma Lens

It is possible to use the technique of plasma wakefield acceleration in a broader context than to simply accelerate particles. In particular, we are able to make deliberate use of betatron motion to both improve the quality of particle-beam focusing devices and to significantly decrease the spatial requirement of existing beam focusing technology.

We showed above that the transverse wakefield within the ion column results in the oscillation of electrons within the particle beam about the central axis. If, instead of generating a long filament of plasma, we generate a small ‘‘blip’’ of plasma, the transverse wakefield dynamics become the dominant mode of motion for the electron beam. Rather than prioritizing the capability of plasma to accelerate electrons longitudinally, this design makes use of electron betatron motion to decrease the overall beam spot size.

In particular, this study focuses on the plasma lens design proposed in 2019 by C.E. Doss et al. [28, 36], which makes use of a plasma in the same underdense blowout regime as is used for PWFA. This design allows the use of the same laser system as used to ionize plasma filaments for PWFA, and is designed to require no external current, increasing its repeatability and ease of implementation.

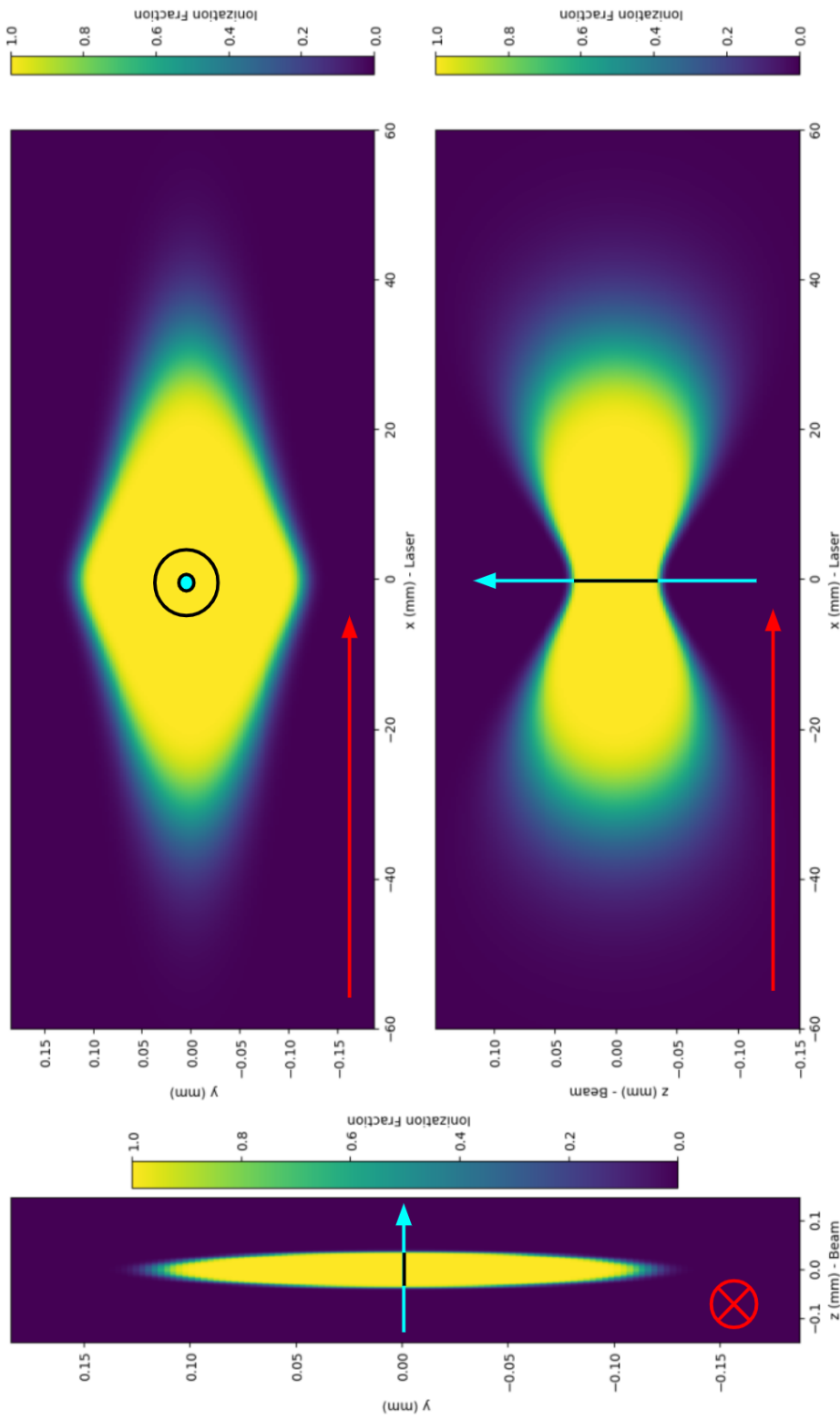


Figure 3.1: Planar cross-sections of plasma lens profile, with electron beam trajectory marked in cyan and laser trajectory marked in red. Clockwise from left:  $y - z$  plane (side view),  $x - y$  plane (front view),  $x - z$  plane (top view).

A plasma lens can focus a relativistic electron beam hundreds of times more powerfully than a conventional quadrupole magnet, in a distance hundreds of times shorter. This is best illustrated by comparing the focal lengths of the underdense plasma lens with quadrupole electromagnets as well as permanent quadrupoles:

<i>Focusing Element</i>	<i>Parameter</i>	$K$ (m <sup>-2</sup> )	$L$ (mm)	$f$ (cm)
Quadrupole Electromagnet	$G = 1$ T/m	0.3	180	1000
Permanent Quadrupole	$G = 500$ T/m	150	8.2	81
Underdense Plasma Lens	$n_p = 10^{17}$ cm <sup>-3</sup>	88400	0.34	3.3

Table 3.1: Comparison between focusing elements of a 10 GeV electron beam [28], normalized such that  $\sqrt{K} \times L$  is equivalent for each optic.

The focusing strength  $K$  of all of the above is determined by a characteristic parameter of the optic, and satisfies Hill's Equation:

$$r'' = -Kr \quad (3.27)$$

The focusing strength of both quadrupole magnets is determined by the magnetic field gradient  $G$ , and by the plasma density  $n_p$  in the case of the plasma lens.

Even when compared to permanent quadrupole magnets, which are significantly more powerful than quadrupole electromagnets, a plasma lens provides superior focusing in a significantly smaller space. Moreover, since the focusing strength of a plasma lens is dependent on the density of the gas from which it is ionized, the plasma lens can be easily tuned as needed to match any experimental setup.

Furthermore, the transverse force on an electron in a plasma wake depends only on  $r$ , as shown in Eq. 3.25, and thus focusing due to the plasma lens is radially-symmetric about the axis of beam propagation. Since the magnetic field of a quadrupole magnet causes defocusing of the electron beam perpendicular to the axis of focus, more than one is required to improve overall beam focus. The symmetry of a plasma lens's transverse focusing force dictates that only one lens is required for optimal focusing.

# Chapter 4

## Laboratory Optics

### 4.1 Ultrashort Laser Pulses

In order for a laser to ionize a plasma from neutral gas, a single laser pulse needs to be significantly intense. The extremely-short pulse length of an ultrashort laser naturally results in an extremely-high total power, since the average power of a laser pulse with energy  $E$  and pulse length  $\Delta t$  is given as

$$P = \frac{E}{\Delta t} \quad (4.1)$$

Ultrashort lasers are capable of extremely-high peak power values for even small energies.

#### 4.1.1 Bandwidth Analysis of Ultrashort Lasers

Lasers with a wide bandwidth are necessary to generate ultrashort pulses. The infrared laser oscillator used in the CU-WARG lab outputs laser light with a central wavelength of 800 nm and a bandwidth of 40 nm [37] at Full-Width at Half Maximum (FWHM), corresponding to frequencies ranging from approximately 340 GHz to 417 GHz. The overall range of output frequencies is centered at 375 GHz and is Gaussian in shape, with a standard deviation  $\sigma_\omega \approx 32.2$  GHz. We can express this as a Gaussian function in the frequency domain, normalized so that its integral over all frequencies evaluates to one:

$$g(\omega) = \frac{1}{\sigma_\omega \sqrt{2\pi}} e^{-\frac{(\omega-\mu)^2}{2(\sigma_\omega)^2}} \quad (4.2)$$

Here the central frequency  $\mu$  is 375 THz, corresponding to the central wavelength of 800 nm. To evaluate this in the time domain, we perform an inverse Fourier transformation:

$$\begin{aligned}
f(t) &= \int_{-\infty}^{\infty} g(\omega) e^{i\omega t} d\omega \\
&= \frac{1}{\sigma_{\omega} \sqrt{2\pi}} \int_{-\infty}^{\infty} e^{-\frac{(\omega-\mu)^2}{2(\sigma_{\omega})^2}} e^{i\omega t} d\omega
\end{aligned} \tag{4.3}$$

Evaluating this integral gives an expression for the shape of the pulse in the time domain:

$$f(t) = e^{-\frac{(\sigma_{\omega})^2 t^2}{2}} e^{i\mu t} \tag{4.4}$$

This function has two component parts: the complex exponential, which represents the carrier frequency, and the Gaussian pulse envelope. If we rewrite this to have the canonical form of a Gaussian function, we find that the standard deviation in the temporal domain is

$$\sigma_t = \frac{1}{\sigma_{\omega}} \approx 31.1 \text{ fs} \tag{4.5}$$

Thus the broad bandwidth of output frequencies from the infrared oscillator corresponds to a laser pulse with a FWHM of  $\approx 73.2$  fs. As the pulse undergoes amplification as described in Section 4.1.2, the material properties of the amplification medium amplify the central laser frequencies to a greater degree than those on the fringe through a process called *gain narrowing*, which increases the pulse length of the amplified laser to 40 fs.

### 4.1.2 Chirped-Pulse Amplification

Chirped pulse amplification (CPA) begins by generating an ultrashort pulse using a mode-locked laser, which is projected onto a diffractive grating, placed at an angle relative to the laser propagation axis. Two converging lenses are placed downstream of this grating, which impart a *chirp* to the overall pulse, with the time derivative of the pulse's frequency now nonzero [38]. The pulse reflects off of a second, identical diffractive grating and back to the first. Over this process, the portions of the laser with the largest wavelength travel a greater path length than those with the smallest. This has the effect of significantly increasing the pulse duration, or “stretching” of the pulse by many orders of magnitude. The energy of the pulse is conserved through stretching, and so the average power of the laser pulse attenuates proportional to the increase in pulse duration.

Now that the pulse is outside of the ultrashort regime, it falls below the damage threshold for optical components and can be easily manipulated. The pulse is then directed through one or more amplifier assemblies, which massively increase the energy in the pulse. Following amplification, the pulse is recompressed to the ultrashort regime via a second diffractive grating pair. Now that the pulse energy is much higher, a return to the ultrashort regime results in enormous peak pulse power.

## 4.2 Laser System

To achieve the extreme intensity required to laser-ionize plasma, our laboratory uses Chirped-Pulse Amplification as described above, as well as a specialized beam control system. The main beam is an 800 nm infrared pulse generated by a Ti:Sapphire oscillator. For maximal intensity, we use an ultrashort pulse, with a pulse duration between 40 and 55 femtoseconds and an output energy between 1 and 5 nJ.

The seed pulse is stretched via diffractive grating and directed through a series of amplifiers, beginning with a regenerative amplifier supplied with energy by a 523 nm ND:YAG pump laser, where it is amplified within a cavity until a Pockel cell allows it to leave the resonator. It then propagates through the first of two multipass amplifiers, where it is passed through a second Ti:sapphire crystal, pumped by the same laser as the regenerative amplifier.

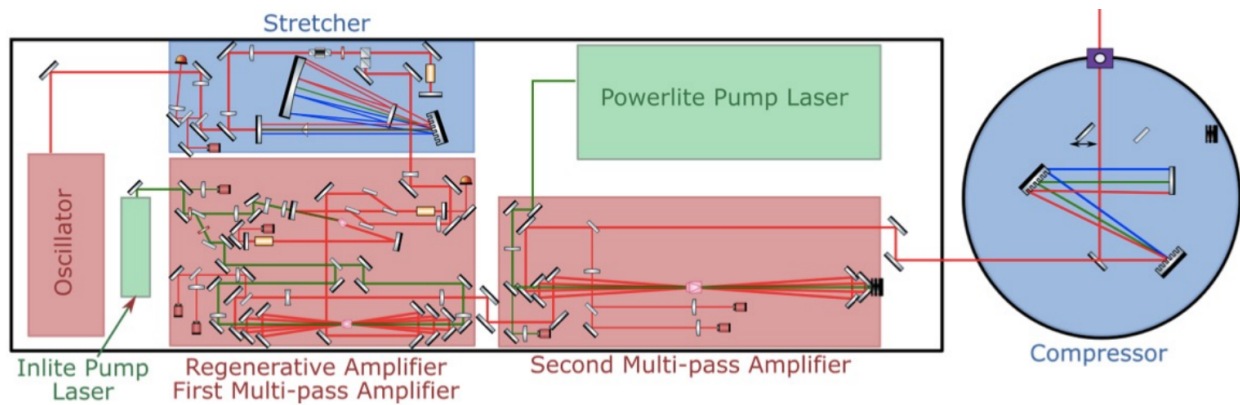
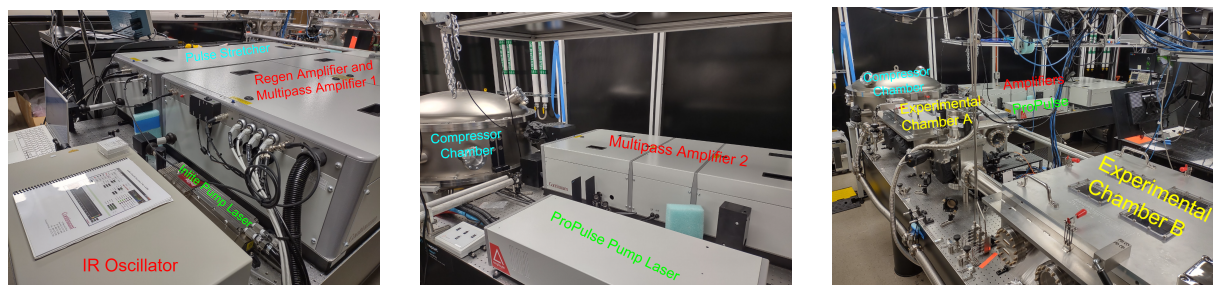


Figure 4.1: Schematic of WARG Lab Centaurus Laser System

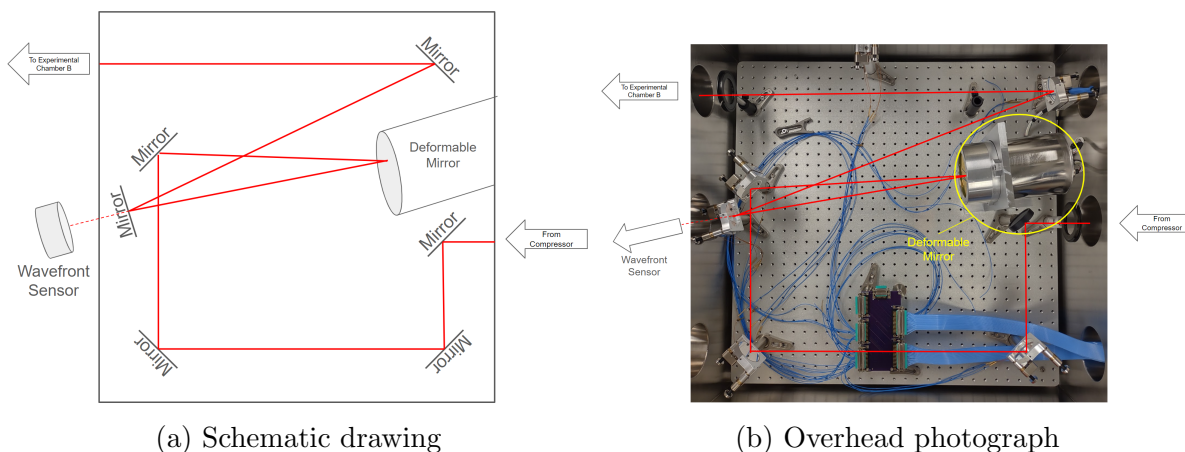
It then propagates through a second multipass amplifier with a larger Ti:sapphire amplifier crystal. In this chamber, energy is added using a more powerful ND:YAG pump laser, resulting in a final pulse energy of around 500 mJ. The stretched, amplified pulse then enters a vacuum chamber for recompression, after which the laser pulse has a peak power on the order of 10 TW. At this point, the pulse energy is high enough that, once the pulse returns to the ultrashort regime, it is powerful enough to ionize air, and so the chamber is kept under vacuum.



(a) Seed laser and first-stage amplifier (b) Second-stage amplifier and compressor (c) Experimental Chambers

Figure 4.2: Photographs of CU-WARG Centaurus Laser system

After recompression, the laser is directed into the first of two experimental vacuum chambers, Experimental Chamber A, which contains a deformable mirror used to correct wavefront aberrations introduced to the laser as part of the amplification process (see Section 4.2.1 below). A wavefront sensor is placed outside of the chamber, which uses leakage light from a mirror installed immediately after the deformable mirror to monitor the pulse wavefront. The corrected beam is then directed into Experimental Chamber B, which contains the experimental designs detailed in Chapter 6.



(a) Schematic drawing

(b) Overhead photograph

Figure 4.3: Detail of Experimental Chamber A, containing deformable mirror for wavefront-correction.

### 4.2.1 Wavefront Optimization

Much of our analysis makes the assumption that the laser beams we deal with have an ideal transverse intensity profile and flat wavefront throughout the beam's path of propagation. In reality, however, this is not the case, as multiple factors can increase aberrations in the beam. All optical components, even brand-new ones, exhibit microscopic imperfections which cause

divergence from an ideal wavefront. Furthermore, interaction with any transmissive optic with non-uniform thickness will cause a deviation from global phase coherence, even if manufacturing imperfections are not present.

To demonstrate this, we consider an ideal lens of non-negligible thickness. Within the body of the lens, the laser light travels at a phase velocity  $v_p$ , determined by the material of the lens:

$$v_p = \frac{c}{n} \quad (4.6)$$

Here  $n$  is the index of refraction of the lens. Light at the edges of the lens will travel through the lens for a shorter time than light at the center of the lens, and will thus travel at  $v_p$  for a shorter time. This results in a differing optical path length, and thus a nonzero difference in phase, for these two rays. Furthermore, the focused rays no longer all cross the optical axis at the focal plane, diverging and resulting in spherical aberration of the pulse. This is generally unavoidable and increases the divergence from an ideal profile as the beam propagates.

The laser pulse inevitably accrues a number of phase aberrations as a result of interaction with all the components involved in the amplification process. To correct these, we make use of a *deformable mirror*, which gives our lab the ability to re-flatten the wavefront before it reaches our experimental setup.

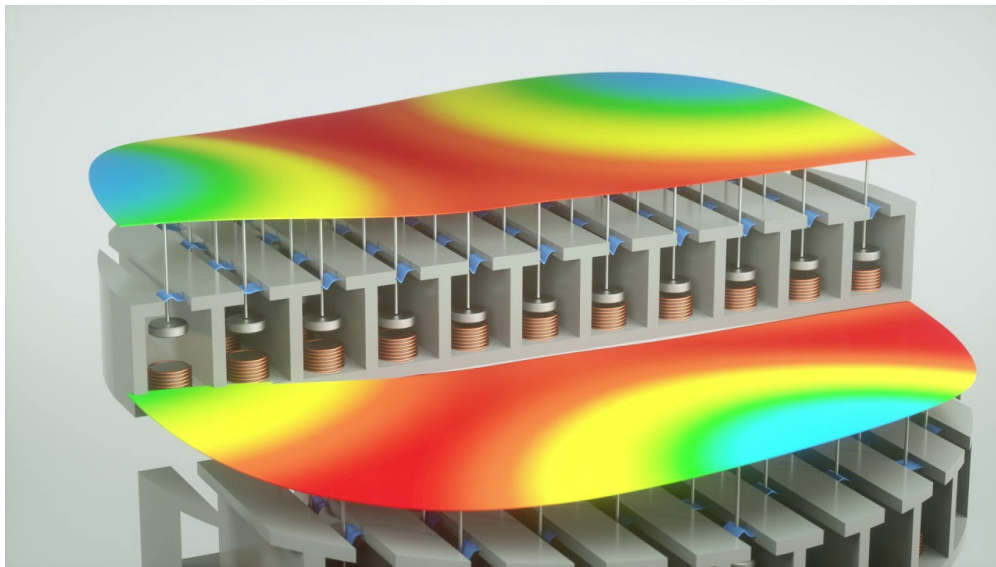


Figure 4.4: Cross-section of deformable mirror displaying piston control of mirror surface.

The deformable mirror consists of a reflective surface connected to 38 pistons with a wide range of motion. After the beam reflects from the mirror, a wavefront sensor outside of the experimental chamber measures leakage light and communicates with the mirror to

correct wavefront aberrations in the main laser beam and to produce a flatter wavefront for use in the main experimental chamber. This is able to make the beam much more globally coherent, to the point where the phase difference between any two given wave packets of the laser is much less than the laser's wavelength ( $\varphi \ll \lambda$ ).

### 4.3 Gaussian Optics

In ray-tracing optics, a laser focuses to an infinitesimally-small point. This is very useful for designing and characterizing large-scale optical schema, but lacks precision, especially concerning the region immediately surrounding the focal plane of the lens. As our experiment requires fine control over the dimensions of a focused laser beam, a more detailed model is required.

We can make use of a Gaussian optical system to model and diagnose our laser as it propagates. Though more complicated than a ray-tracing model, it remains robust and relatively simple in comparison to more detailed methods of optical analysis. The behavior of most laboratory lasers complies very well with the Gaussian optical model, even if their intensity profile is not exactly Gaussian [39].

Gaussian optics assumes that laser pulses are characterized by a radially-symmetric Gaussian distribution, and have an intensity profile characterized as

$$I(r, z) = I_0(z)e^{-\frac{2r^2}{w(z)^2}} \quad (4.7)$$

where  $I_0(z)$  is the peak pulse intensity along its axis of propagation, and  $w(z)$  is the beam waist as described later in Eqn. 4.9. Though the on-axis intensity of the pulse varies with both  $I_0(z)$  and  $w(z)$ , the radially-integrated power remains constant along  $z$ .

$$\begin{aligned} P &= \iint_S I(r) dA \\ &= \int_0^\infty \int_0^{2\pi} I_0(z)e^{-\frac{2r^2}{w(z)^2}} r d\theta dr \\ &= 2\pi I_0(z) \int_0^\infty e^{-\frac{2r^2}{w(z)^2}} r dr \\ &= 2\pi I_0(z) \left( \frac{w(z)^2}{4} \right) \\ &= \frac{\pi}{4} I_0(z) w(z)^2 = \text{const.} \end{aligned} \quad (4.8)$$

As the beam propagates, its radius is described by

$$w(z) = \sqrt{w_0^2 + \left( \frac{z\lambda}{\pi w_0} \right)^2} \quad (4.9)$$

where  $\lambda$  is the wavelength of incident light,  $w_0$  is the smallest radius of the beam, and  $z$  is the distance of the laser from the point of smallest focus (i.e.  $w(z = 0) = w_0$ .) We can also describe this in terms of its Rayleigh length  $z_R$ , where

$$z_R = \frac{\pi w_0^2}{\lambda} \implies w(z) = w_0 \sqrt{1 + \left(\frac{z}{z_R}\right)^2} \quad (4.10)$$

The Rayleigh length describes the distance over which the beam can propagate without diverging significantly [40]. For values of  $|z| \lesssim |z_R|$ , the waist grows quadratically as  $w(z \simeq z_R) \approx w_0(1 + \frac{1}{2}(z/z_R)^2)$ ; in the limit where  $|z| \gg |z_R|$ , the waist grows linearly:  $w(z \gg z_R) \approx (w_0/z_R)z$ .

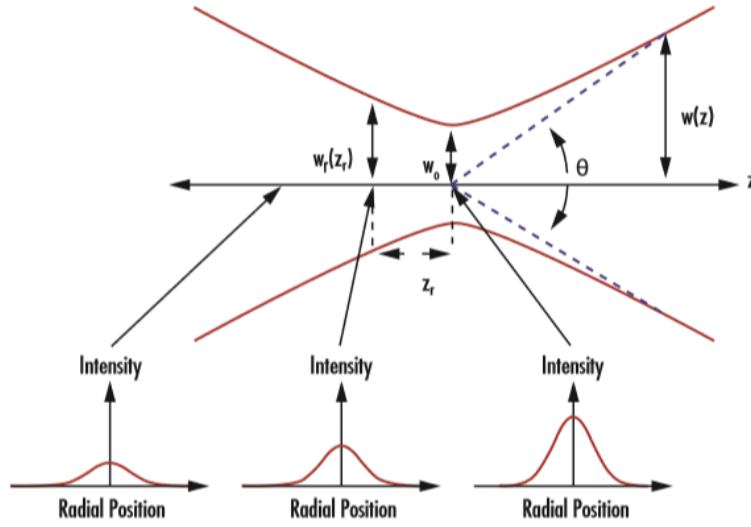


Figure 4.5: Evolution of a Gaussian beam near the beam waist. [40]

The beam waist  $w_0$  can be evaluated from the beam divergence angle. For a converging lens, the beam waist occurs at a distance away from the lens equivalent to the lens's focal length  $f$ , which, in addition to the beam's radius at the lens plane  $r_0$ , gives the divergence angle:

$$\theta_{div} = \tan^{-1}\left(\frac{r_0}{f}\right) \quad (4.11)$$

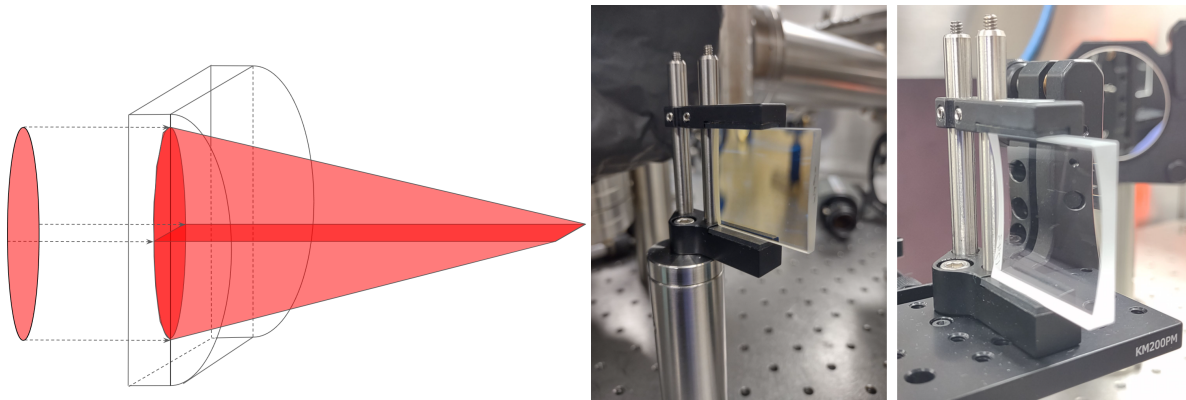
This allows us to fully-define the beam waist at its smallest point as

$$w_0 = \frac{\lambda}{\pi \theta_{div}} = \frac{\lambda}{\pi \tan^{-1}(r_0/f)} \quad (4.12)$$

This is a simple and robust metric which gives a precise characterization of an evolving beam near its focus.

### 4.3.1 Cylindrical Lenses

In order to ionize a plasma of the proper dimensions for a plasma lens, we need a long elliptical beam focus. The best way to achieve this without inducing significant beam aberration is through the use of cylindrical lenses. Unlike spherical lenses, which focus an incoming beam to a single point, cylindrical lenses focus along one axis transverse to the beam, without affecting the beam in the other axis. The image at the focal plane is a line whose length is determined by the unfocused beam diameter.



(a) Ray-trace of converging lens.

(b) Detail photos of cylindrical lenses: +200mm converging (left) and -100mm diverging (right).

Figure 4.6: Schematic and photos of cylindrical lenses. The ability to focus along a single transverse axis is integral to the lens design presented here.

The optimal dimensions of a plasma lens require that its thickness be significantly less than the distance a beam electron travels in a single betatron period. While it is certainly possible to achieve such a precise beam focus using custom-manufactured lenses, a main goal of this project is to generate a plasma lens using inexpensive off-the-shelf lenses.

Two or more cylindrical lenses, oriented  $90^\circ$  relative to each other, form the desired beam shape when properly positioned within the beam path. The final beam dimensions are determined by the focal length of the upstream lenses, as well as the initial beam size, as dictated by Eq. 4.9. We are also free to choose lenses of differing focal lengths for each transverse axis, allowing for an asymmetric final focus.

# Chapter 5

## Visible Laser Experimental Tests

### 5.1 Two-Lens Experimental Design

Prior to using the Ti:sapphire laser system, we conducted two different experiments in open-air with easy-to-use low-power lasers. The first used a REO R-30989 Helium-Neon (HeNe) laser, which emitted 633nm red light at an output power of 2 mW. The use of this laser presented several challenges to accurately diagnose beam alignment through our lenses, as we discovered that the initial laser profile had extremely heavy diffraction patterns. We attempted to mitigate this through the use of a pinhole spatial filter, though this was insufficient to fully correct the poor beam profile.

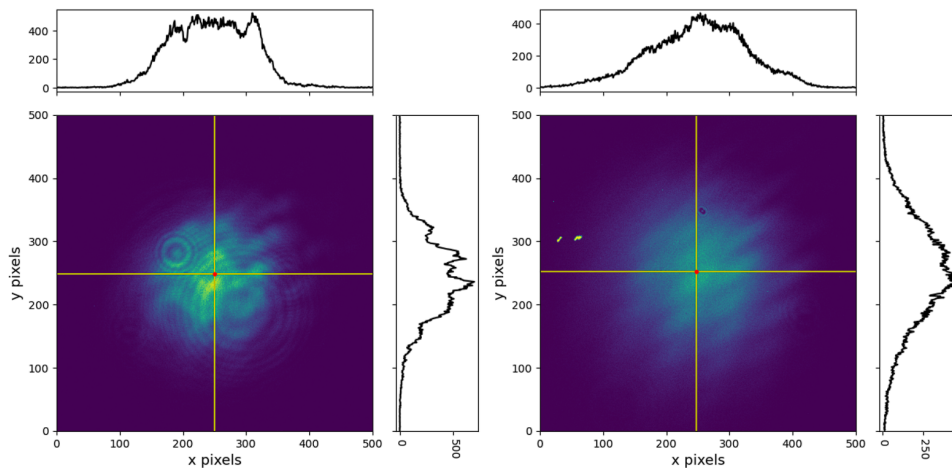


Figure 5.1: Intensity profile of HeNe laser before (left) and after (right) spatial filtering.

We decided that it would be more useful to use a ThorLabs PL-210 520nm green diode laser to conduct our analysis. The green diode laser had significantly less inherent diffraction, but required 5 meters of beam propagation before an acceptable Gaussian profile was

reached. In order to do this, we allowed the laser to propagate through air a combined total of 5.2 meters along the entire length of the experimental table and back. The beam was then magnified by a 10x beam expander to better emulate the laser profile used at SLAC.

In order to verify both the action of the cylindrical lenses and their compliance with Gaussian optical models, the initial experiment used two converging cylindrical lenses, one with a focal length of 700 mm and one with 200 mm, placed such that their focal planes were incident. A camera is used to capture the final beam focus. In order to fully-map the smallest waist of the beam, the camera is installed on a micrometer stage with a 20-mm range of travel.

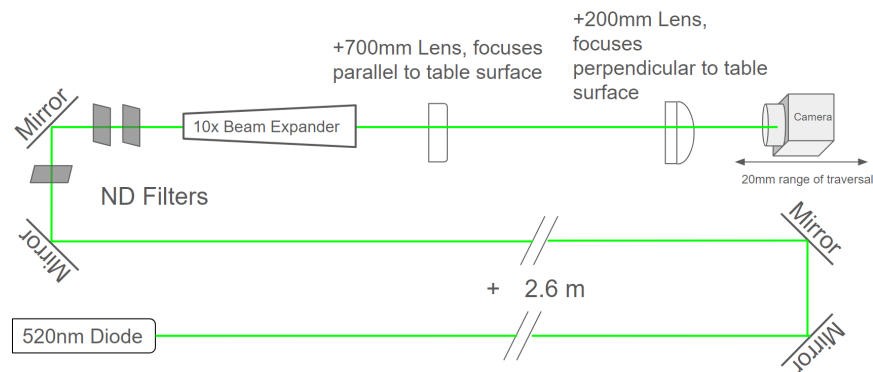


Figure 5.2: Schematic of two-lens experimental setup.

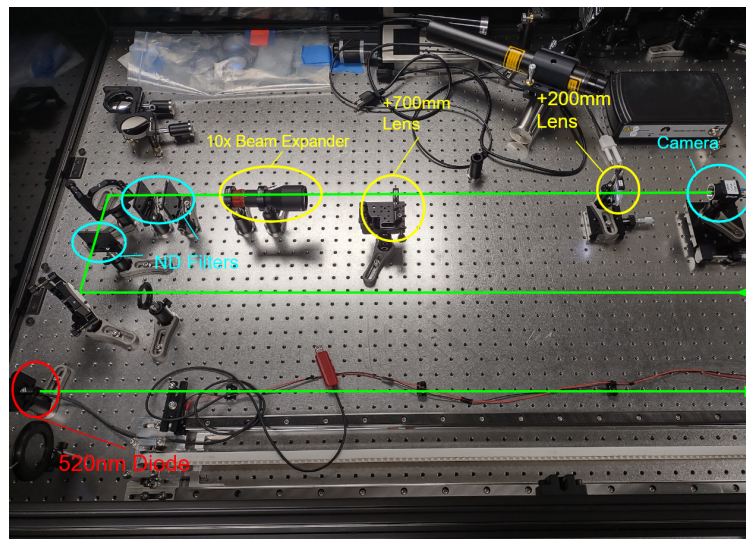


Figure 5.3: Overhead photo of two-lens experimental setup.

### 5.1.1 Experimental Considerations

It is common laboratory practice to install a neutral-density (ND) optical filter on the barrel of a camera used to directly image laser profiles. ND filters are characterized by an optical density parameter  $d$ , and decrease the intensity of incident light by a factor of  $10^{-d}$ . These components are vital in preventing overstimulation and damage of the sensitive camera imaging chip. However, the installation of the camera in the region where the beam waist occurs can cause derangement of the laser beam. This is illustrated by a ray-trace diagram of a converging laser interacting with an ND filter:

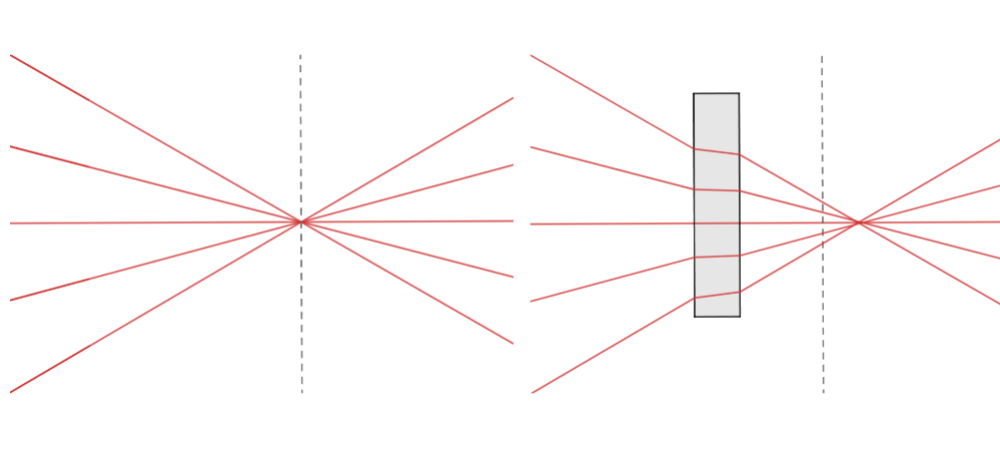


Figure 5.4: Ray-trace diagram for a converging lens with no ND filter (left) and with an ND filter (right). The dashed line denotes the nominal focal plane.

This disrupts our data in two ways. First, the improperly-converging rays cause the final captured image to be blurry or otherwise out of focus. More severely, the converging laser no longer complies with the Gaussian optical model described in Section 4.3, resulting in inaccurate waist measurements. This is highly detrimental to our ability to characterize a precise beam focus. Thus, to avoid damage to the camera’s imaging chip, a series of ND filters with a combined optical density of 5.3 were installed just upstream of the 10x beam expander, at the last point where a collimated beam was guaranteed.

### 5.1.2 Data Collection Procedure

In both experiments, we measured the final beam shape by directly imaging the beam onto a camera. For each lens in the case of the two-lens experiment, or for the combined lens system in the three-lens experiment, we first performed a coarse scan of 21 data points, collected over the entire 20mm traversal range of the camera micrometer stage in 1mm increments. This allowed us to evaluate the overall compliance with Gaussian optics, as well as determine more precisely where within the range of traversal the beam waist fell.

We then took a second data scan of 21 data points with a smaller increment size, centered on the location of the beam waist as determined by the coarse scan. The step size of this varied depending on the Rayleigh length of the lenses in use, given by Eqn. 4.10. For the second scan, the step size fell between  $250 \mu\text{m}$  for the 200mm converging lens and  $500 \mu\text{m}$  for the 700mm converging lens. This higher-resolution scan gave an acceptably precise location of the beam waist.

After precisely locating the smallest focus of the beam, we took a high-resolution scan of 41 data points, centered on the location of the beam focus as determined by the second scan. This scan would provide our best results for the beam profile, and ranged in increment size from  $10 \mu\text{m}$  for the 200mm lens to  $150 \mu\text{m}$  for the combined three-lens system.

Captured images for each of these datasets was analyzed using a homebrew beam analysis package, providing overall beam trends and data-fitting.

### 5.1.3 Results

This experiment verified the compliance of our cylindrical lens scheme with our expectations from the Gaussian optical model. Both the +200mm and +700mm lenses displayed beam divergence which was linear for values of  $z$  much greater than the Rayleigh length.

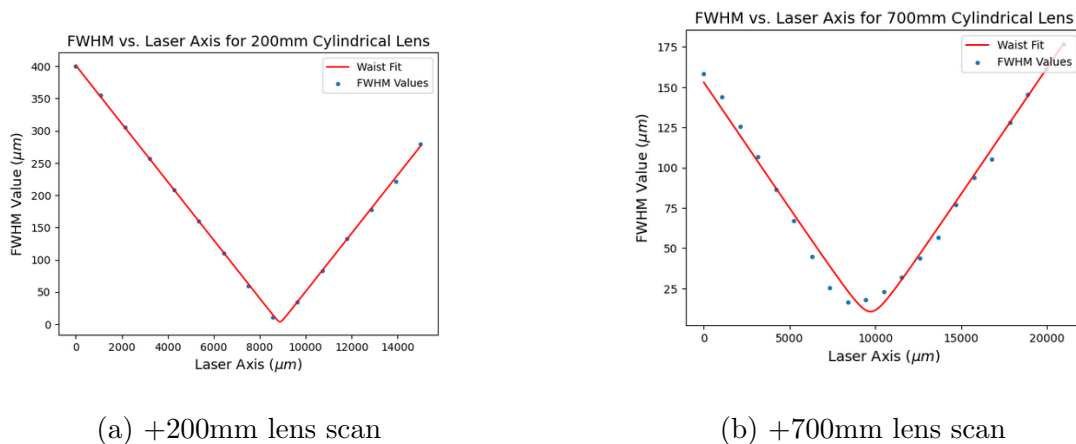
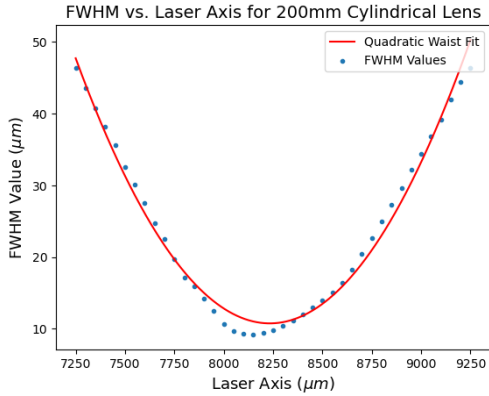
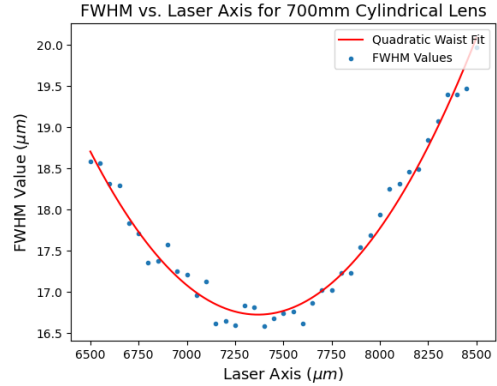


Figure 5.5: Coarse scan of the evolution of laser beam waist near the focal plane of individual lenses. Each dataset consists of 21 images collected with a 1 mm step size.

Nearer to the waist, the beam evolution is quadratic about the central point. This data set was fit to the Gaussian waist equation (Eq. 4.9).



(a) +200mm lens scan,  $z_R \approx 118\mu\text{m}$



(b) +700mm lens scan,  $z_R \approx 1450\mu\text{m}$

Figure 5.6: Fine scan of the evolution of laser beam waist near the focal plane of individual lenses. Each dataset consists of 41 images collected over a 2mm range with a  $50\mu\text{m}$  step size.

When combined, the lenses continued to perform as expected, though we were able to deduce from the relative location of the waists for the +200mm and +700mm lenses that the two lenses were not reaching the waist at the same value of  $z$ , and that they were thus not ideally-spaced relative to each other. These were, however, determined to be simple enough to install and align that we continued onto the explicit lens parameters given by Doss.

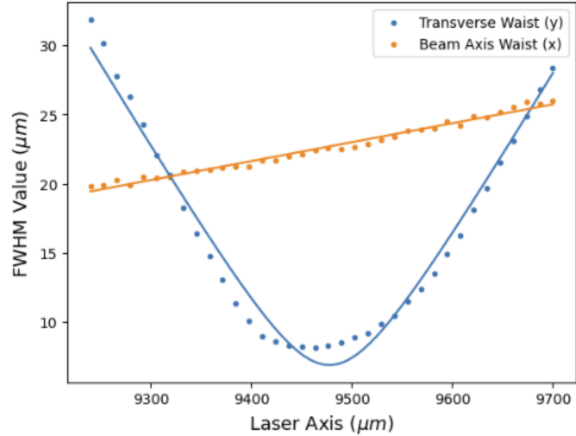
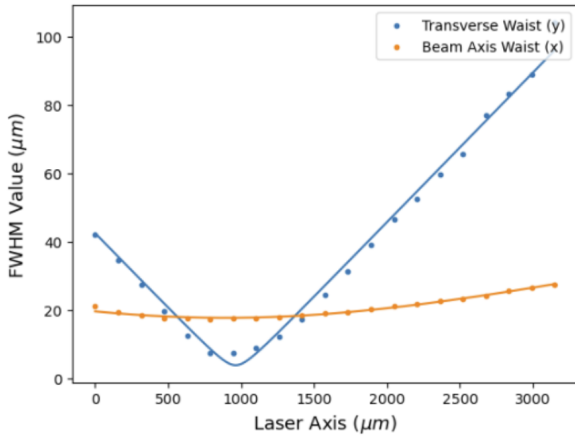


Figure 5.7: Scans of the evolution of laser beam waist near the focal plane of the orthogonally combined +200 mm and +700 mm lenses. Coarse scan (left) consists of 21 data points collected over a 3mm range in  $30\mu\text{m}$  steps. Fine scan (right) consists of 41 data points collected over a 1.6mm range in  $40\mu\text{m}$  steps.

## 5.2 Three-Lens Experimental Design

The initial experiment was augmented to include a diverging cylindrical lens with a  $-100$  mm focal length, in accordance with the design proposed in Doss 2023 [28]. The design of this is the same as the above experiment through the  $10\times$  beam expander, but varies in where the lenses are installed. Rather than positioning the lenses only such that their focal planes are incident, the  $200\text{mm}$  converging lens is placed first, then the diverging  $-100\text{mm}$  lens is placed  $109\text{mm}$  downstream of the converging  $+200\text{mm}$  lens, resulting in an effective focal length of  $2.2\bar{2}$  meters for the combined lens system. The  $700\text{mm}$  lens is placed an additional  $308\text{mm}$  downstream. As before, the combined  $200\text{mm}/-100\text{mm}$  lenses focus along  $x$  and the  $700\text{mm}$  lens focuses along  $y$  as described above. For precise alignment, both the  $-100\text{mm}$  and  $700\text{mm}$  lenses are installed in kinematic tip-tilt mounts allowing precise control of lens pitch in the transverse plane. The diverging lens is also mounted on a micrometer stage with a  $10\text{-mm}$  range of traversal for precise longitudinal positioning.

Doss places the plasma lens  $1117\text{mm}$  downstream of the first cylindrical lens. Our experimental space was too limited to place the camera directly in-line with the lenses, requiring us to place the camera at  $\sim 25$  cm perpendicular to the propagating beam and install a mirror to allow the beam its full required distance. Once again, the camera is installed on a micrometer stage to allow camera scanning along the optical axis.

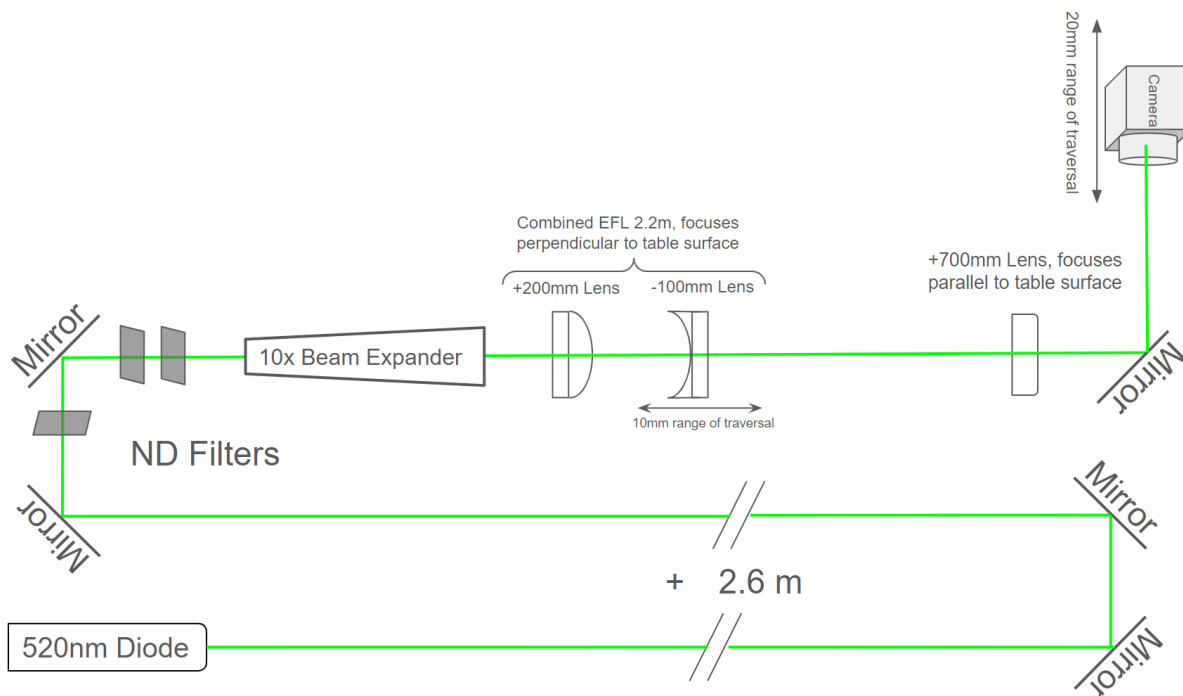


Figure 5.8: Schematic of three-lens experimental setup.

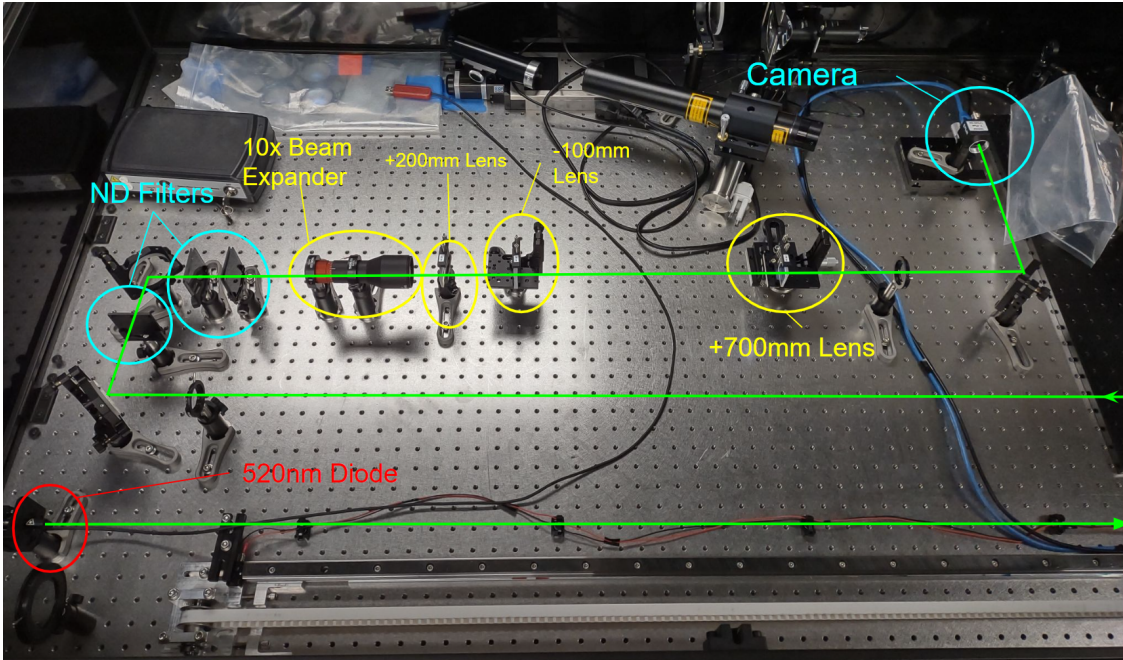


Figure 5.9: Overhead photo of three-lens experimental setup.

### 5.2.1 Data Collection

Alignment was achieved through use of the CU-WARG data acquisition software (DAQ). Following initial alignment through the lenses, we increased the camera gain and exposure time to the point where the image began to saturate. We were then able to find the region of most intense focus through minute adjustments of the lens. After locating this position, the gain was reduced to prevent saturation. Dataset images were collected using the same process detailed in section 5.1.2.

### 5.2.2 Results

We were able to reach several promising conclusions from our initial low-power tests, which informed the design of the next experiment. Most importantly, we found that we were able to generate the predicted beam focus using the three cylindrical lenses. Using direct pixel measurements, we found that the minor axis of the focus was  $\approx 34.5 \mu\text{m}$  with a major axis of  $\approx 124.2 \mu\text{m}$ . The lens proposed in Doss 2023 [28], by contrast, has a minor axis of  $37.4 \mu\text{m}$  and a major axis of  $118.5 \mu\text{m}$ , showing that our beam falls within acceptable deviation from the theoretical prediction. Furthermore, we found that this was achievable without needing to mount any on the lenses onto high-precision micrometer stages, and that diagnosis of aberration was possible solely through observation.

We found also that all three of the cylindrical lenses complied with the Gaussian waist equation when properly aligned. This is highly-promising, as it allows for precise fine-tuning

of the beam waist as necessary.

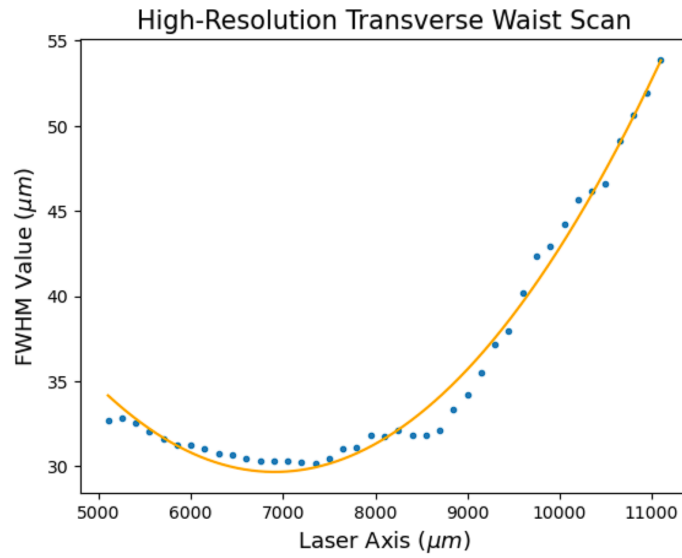


Figure 5.10: Fine scan of the evolution of minor axis of the laser beam waist near the focal plane of the lenses using the 520 nm laser.

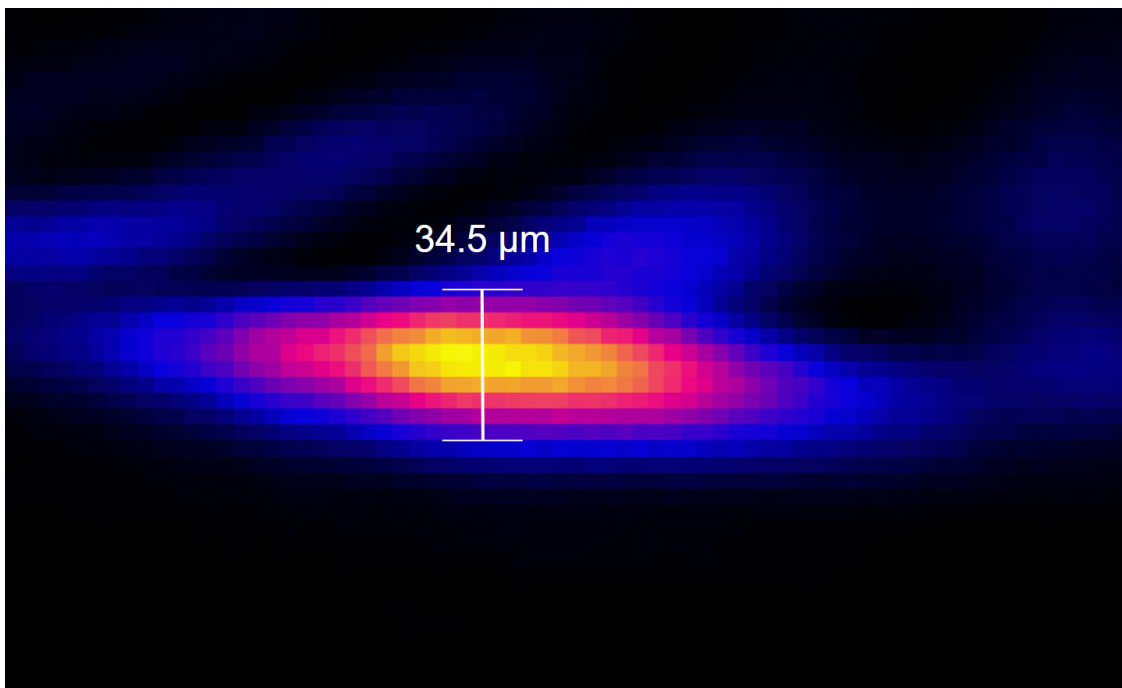


Figure 5.11: Intensity profile of the 520 nm laser at the focus of the three-lens setup.

# Chapter 6

## Infrared Laser Experimental Tests

### 6.1 IR Laser Diode Tests

The next experimental round was conducted in open air inside the experimental vacuum chamber using a Class-3B ThorLabs LDM785 infrared diode with a typical wavelength of 785 nm and an output power of 20 mW. This is done for two reasons. Fine alignment of the main laser can be difficult due to its relatively low repetition rate, and it is simply easier to set up a lower-power CW diode laser in the same experimental space and use it to align all of the optical components relative to each other. From here, we need only align the main laser onto the first optic in this scheme and only minor adjustments are necessary for optimal alignment. Furthermore, all of the experiments discussed in Chapter 5 were conducted using a 520nm green laser. Largely, we do not expect the action of the cylindrical lenses to change significantly with the longer 800nm wavelength of the main laser. However, a material's index of refraction is dependent, albeit weakly, on the wavelength of incident light. This presents a good opportunity to verify that our assumptions regarding lens performance still hold. At both the CU-WARG lab and SLAC, plasma is generated using an 800nm infrared Ti:sapphire laser pulse (See Section 4.2). We chose fused-silica lenses for our experiment, since their index of refraction differs little between 800nm infrared light and the visible range [41], allowing us to use the same lenses between the open-air and vacuum-chamber experiments.

#### 6.1.1 Experimental Design

The IR diode was installed in Experimental Chamber B, and the laser profile was observed to be rectangular, with a length of approximately 3mm and a width of approximately 1.5mm. To better simulate the main laser profile, we manufactured a pinhole with an approximate diameter of 1mm, and then used the same 10x beam expander as the open-air experiments detailed in Chapter 5. The expanded laser was then directed through ND filters with a combined optical density of 7.5 to prevent damage to the camera microchip. The beam then

interacts with the +200mm converging and -100mm diverging cylindrical lenses and allowed to propagate 308 mm to the +700mm cylindrical lens. The beam is then measured by a camera on the same micrometer stage as previously.

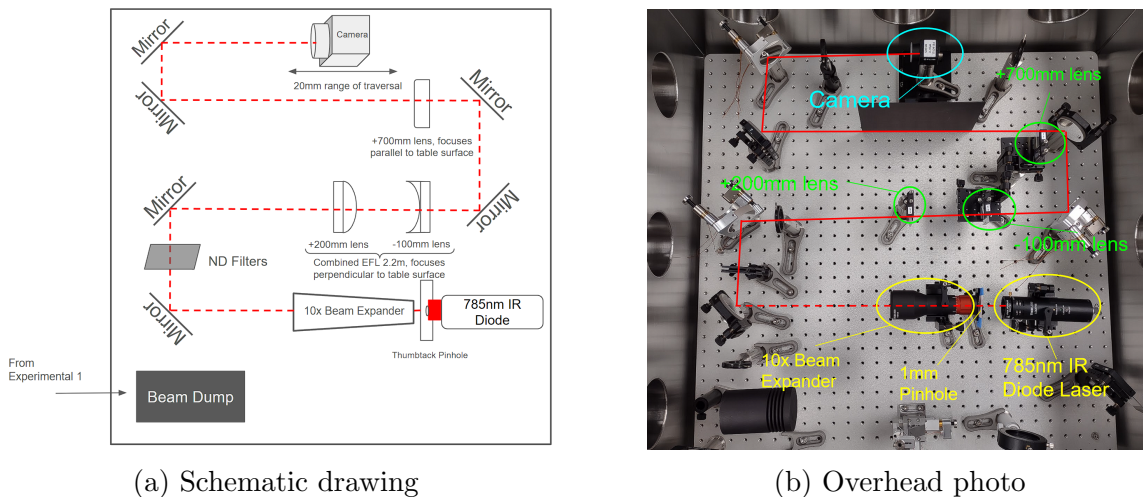


Figure 6.1: IR diode laser experimental setup.

### 6.1.2 Results

After collecting the first dataset, we observed that the final lens had a much wider beam waist and a much longer Rayleigh length than we had expected. Initially, we attributed this to misalignment, but returned the same trend after realignment. Upon further inspection, we determined that the beam diameter was less than the presumed 1cm following the 10x beam expander, as a result of two factors.

The pinhole was manufactured in orange paper using an office thumbtack with a diameter measured to be 1mm. This procedure left an exit burr on the downstream side of the orange paper, which could not be cleanly removed and decreased the effective radius of the laser. The choice to proceed with this pinhole was largely due to time constraints. In addition to the reduced diameter of the pinhole, we observed that the magnification of the 10x beam expander was not precisely 10x, and was likely less. The laser beam post-expander was measured to have a diameter of  $6 \text{ mm} \pm 1 \text{ mm}$ .

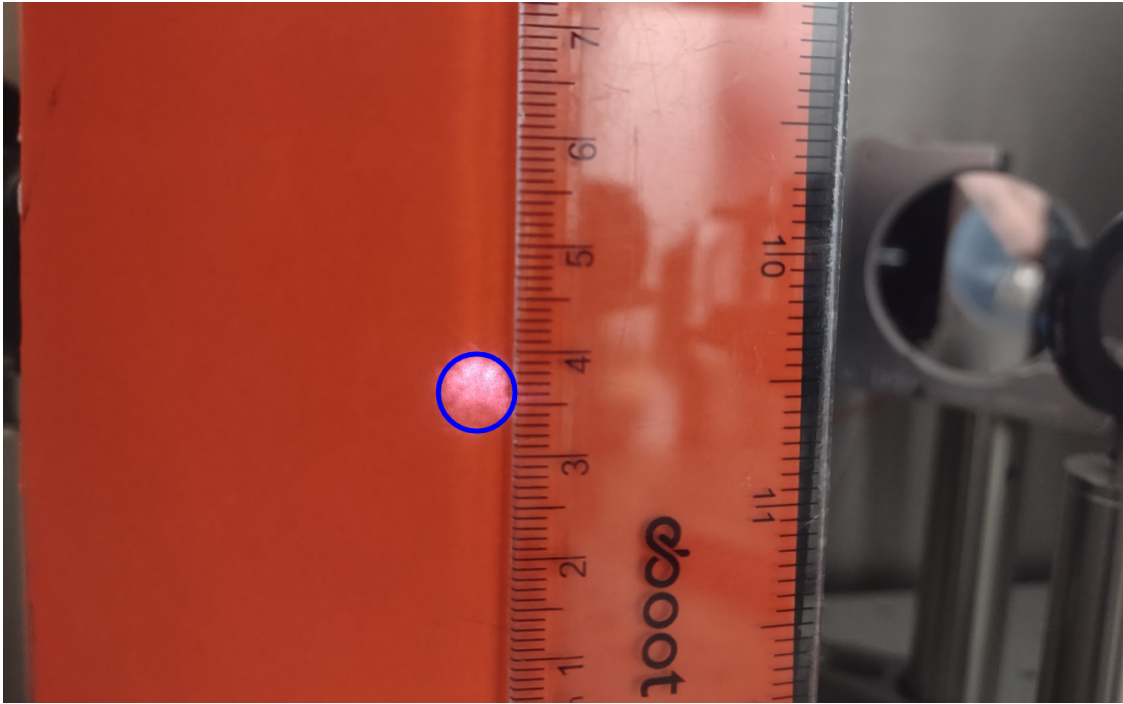


Figure 6.2: Diode laser post-expander. This beam diameter,  $6 \text{ mm} \pm 1 \text{ mm}$ , corresponds to an expected final beam waist of  $61.1 \pm 10 \mu\text{m}$  and a Rayleigh length of  $15 \pm 5 \text{ mm}$ .

Once we identified the issue, we determined that the lenses continued to perform as the Gaussian model predicted they would, and measured a final beam focus of  $76.4 \pm 13.19 \mu\text{m}$ . The uncertainty in our measurement comes from the pixel size of our camera, which is  $3.45 \mu\text{m}$ , added in quadrature with the uncertainty in the diameter of the initial beam. Furthermore, the final beam focus is at an angle with respect to the camera, so the minor axis of the lens is slightly smaller with respect to the captured value. Our measured value is about 15 microns larger than the predicted value of  $61.1 \mu\text{m}$ . With all this accounted for, our measured value of the beam falls within the uncertainty of the predicted value.

Since our data continued to comply with the Gaussian model, we determined that infrared light continued to interact with the lenses as expected, and that we were free to continue with the main laser experiments.

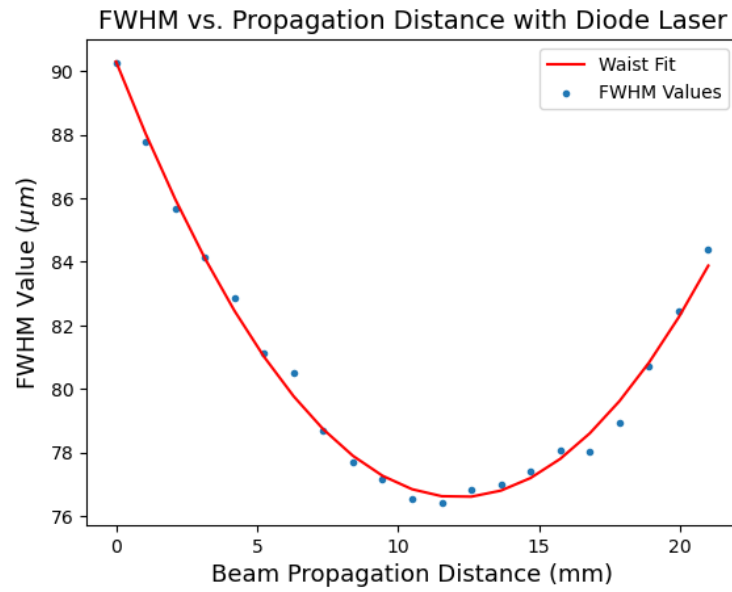


Figure 6.3: Scan of the evolution of minor axis of the laser beam waist near the focal plane of the lenses using the IR diode laser.

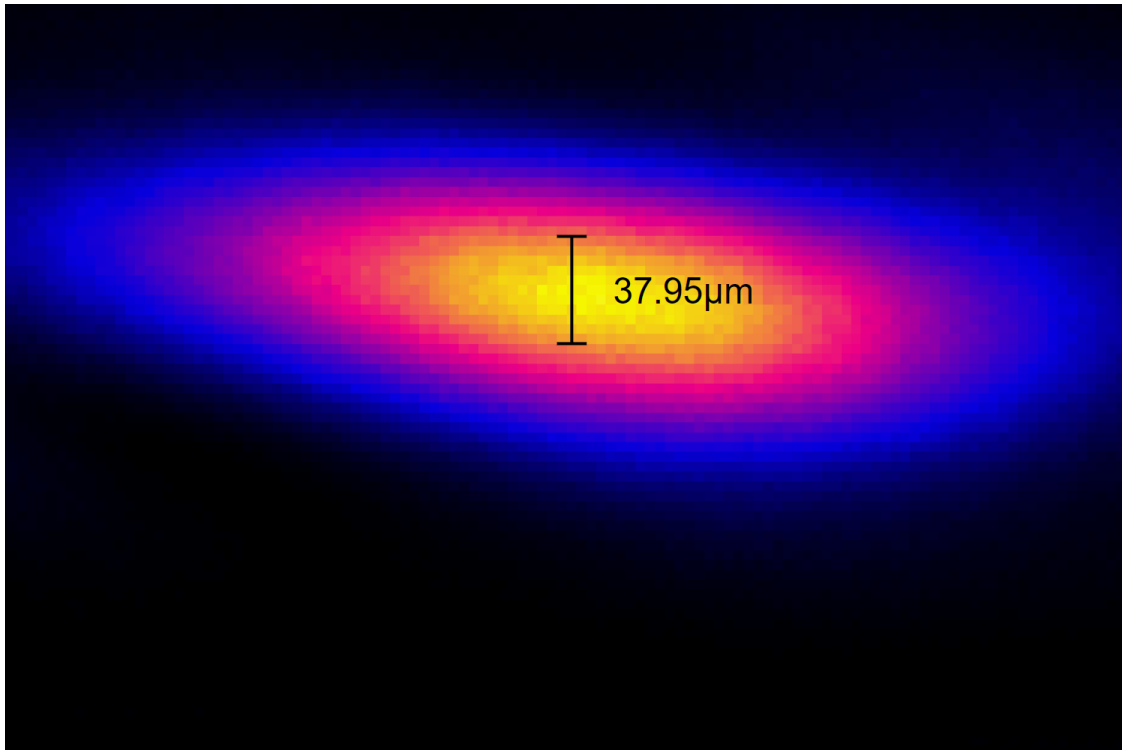


Figure 6.4: Intensity profile of the IR diode laser at the focus of the three-lens setup.

## 6.2 Centaurus Laser Tests

### 6.2.1 Experimental Design

The beam dump is moved from the chamber entrance to allow laser transport from Experimental Chamber A. The mirror previously used in conjunction with the diode laser is moved to allow the main laser to interact with the lenses. Following recompression, the amplified laser pulse has a beam diameter of 30mm. In order to conduct the experiment, which was designed for a beam 10mm in diameter, an alignment iris in Experimental Chamber A was apertured-down to match the desired beam radius.

When aligning the main laser to the lenses, we discovered that the optimal beam waist was upstream of where the camera was installed; the micrometer stage of the camera was moved to be able to fully image the beam waist region. In order to avoid damage to the camera, ND filters were added to increase the optical density from 7 to 11.

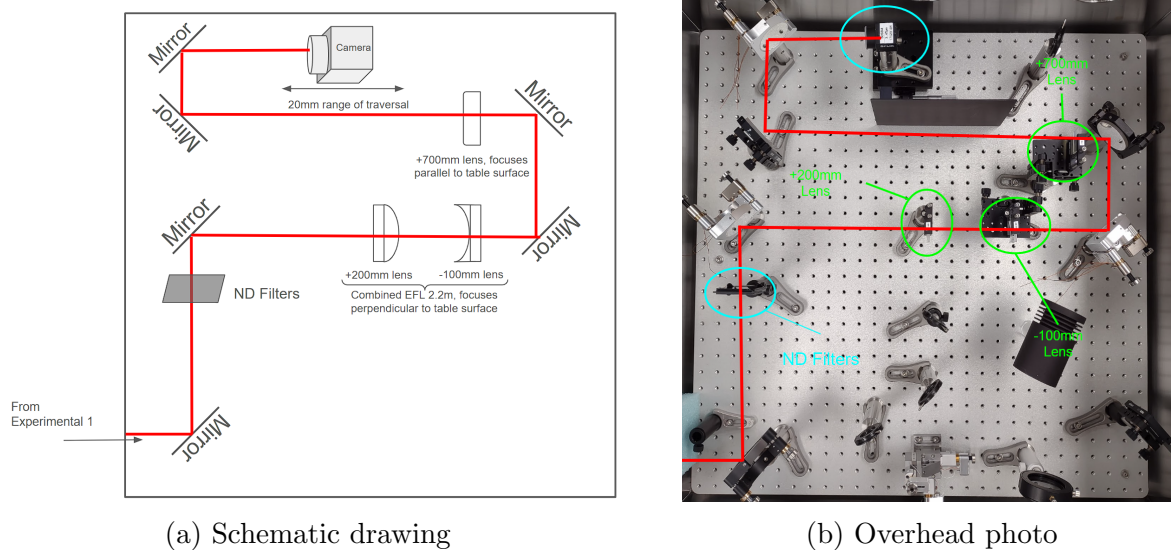


Figure 6.5: Pulsed IR laser experimental setup.

### Intensity Considerations

The open-air tests used a low-power class-2 diode laser with an output power of 0.9 mW. At its smallest focus with our optical design, the irradiance of this is on the order of  $10^{10}$  W/m<sup>2</sup> and falls significantly below the level at which silvered mirrors can be damaged, as per the manufacturer. When using the high-power IR laser, even at a reduced pulse energy of 10 mJ, it is possible for the laser pulse to be focused to a point where its irradiance is high enough to cause dielectric breakdown of mirrors, leading to damage. In order to fit the full required path length of the laser inside of Experimental Chamber B, it was necessary to install several mirrors downstream of the lenses. Prior to using the high-power laser, we had

to evaluate whether our current setup could be used without damaging it.

To this end, we make several assumptions. First, we assume that the laser complies ideally with the Gaussian optical model described in Chapter 4, initially has a circular Gaussian profile, and that interaction with cylindrical lenses only affects the beam radius along their axis of focus. Due to the extremely small transverse size of the focused beam, we will assume that the beam energy is distributed uniformly across the transverse profile. To better model the Centaurus laser in our laboratory, we assume that the laser has a diameter of 10mm before it interacts with the first cylindrical lens, and determine its evolution using Equation 4.9.

The beam intensity is determined by the area of its transverse profile, which we know to be elliptical in shape. Each set of cylindrical lenses causes contraction of one of the axes of the ellipse. We will further assume that every mirror in the beam path sits at a  $45^\circ$  angle relative to the beam path, stretching the  $x$ -component of the ellipse by a factor of  $\sqrt{2}$ . The laser intensity is compiled in the table below, and the mirrors are numbered from 1 to 4 beginning with the first mirror after the -100mm diverging lens, as shown in Figure 6.1b.

	Laser Distance ( $mm$ )	Beam Size ( $mm^2$ )	Intensity ( $W/cm^2$ )
Mirror 1	$121 \pm 1$	44.9	$5.57 \times 10^{11}$
Mirror 2	$260 \pm 1$	37.9	$6.60 \times 10^{11}$
Mirror 3	$753 \pm 1$	4.81	$5.19 \times 10^{12}$
Mirror 4	$877 \pm 1$	1.34	$1.86 \times 10^{13}$

Table 6.1: Laser intensity at 10 mJ pulse energy, assuming an initial beam radius of 5mm.

These all fall well below the upper limit for laser intensity for these mirrors and inform our energy limit for future high-power tests.

### 6.2.2 Results

Our previous experiments had given us a high degree of confidence in the beam’s evolution over the waist region. For an incident beam diameter of 10mm, the Rayleigh length of the final focusing lens is 5mm. Because of this, we opted to collect only a single scan over the micrometer range.

We found that the minor axis of the beam focus reached a width of  $34.5 \pm 3.45 \mu m$  at the waist, which was smaller than the nominal parameters given in Doss by only  $2.9 \mu m$ . This is less than the width of a single pixel in the camera used to measure the laser, and falls within the predicted uncertainty. The major axis of the focus reached a minimum of 3.4 mm, and continued to increase across the dataset. This indicates that the spacing between the +700mm lens and the other two lenses is not optimal, and that the spacing between the +200mm and -100mm lenses may also be incorrect.

We also observed evidence of diffraction in our captured images. These were largely along the minor axis of the beam profile, and switched across the axis as the beam progressed through the waist.

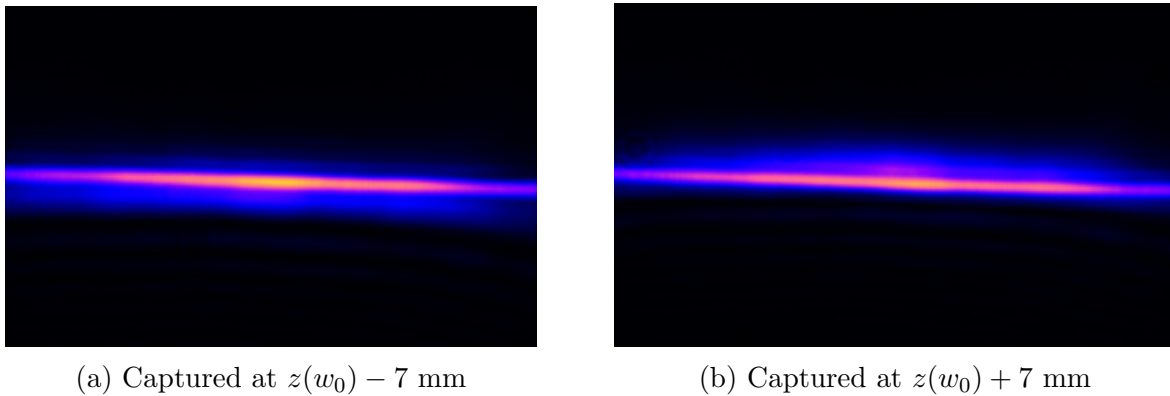


Figure 6.6: Intensity profile of the pulsed IR laser at points equidistant from the focal point,  $z(w_0)$ . Note that diffraction effects shift to opposite sides of the center as the beam progresses through the waist, likely due to a tilt of the vertically focusing lens.

This is likely due to our use of an upstream iris to reduce the beam from a diameter of 30mm to a diameter of 10mm, rather than using a telescope.

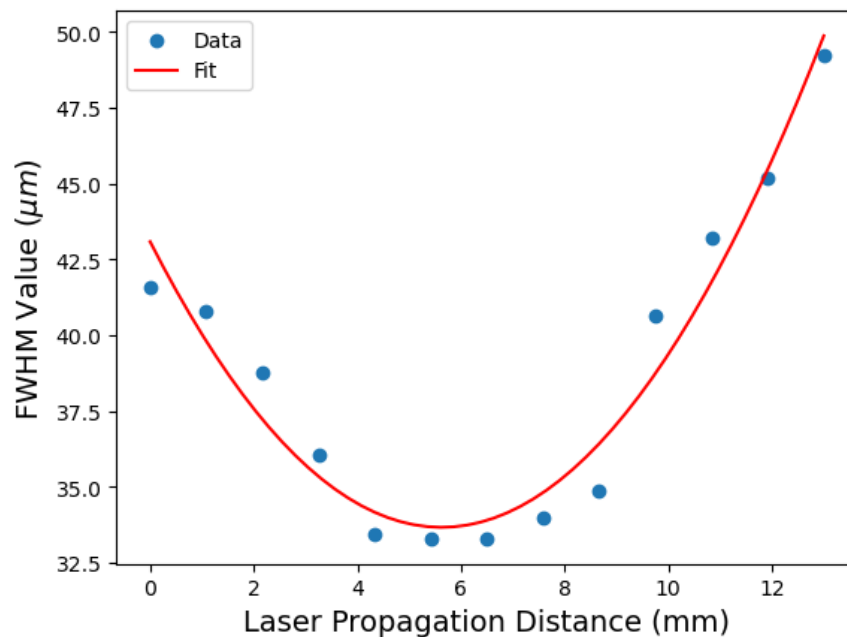


Figure 6.7: Scan of the evolution of minor axis of the laser beam waist near the focal plane of the lenses using the pulsed IR laser.

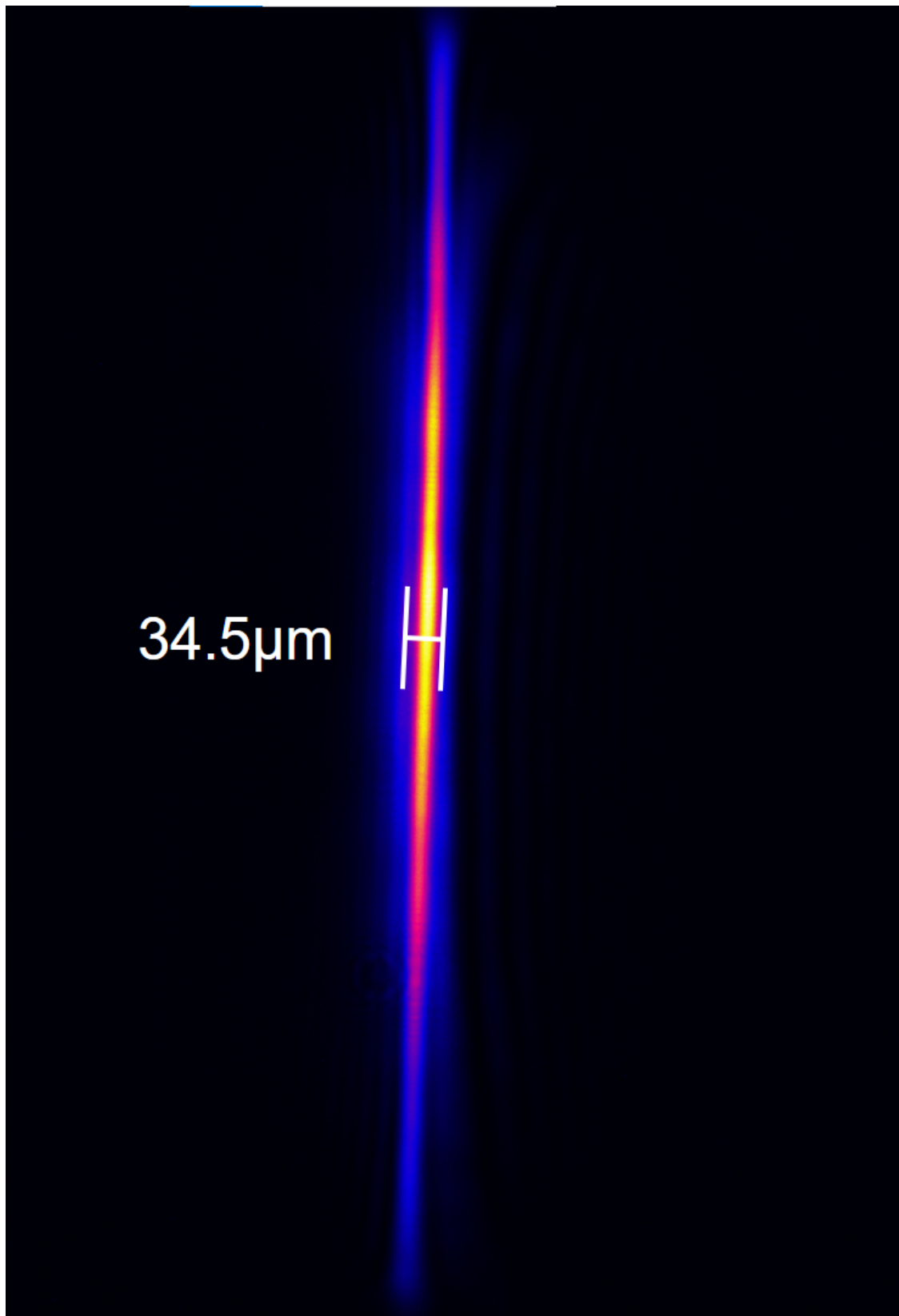


Figure 6.8: Intensity profile of the pulsed IR laser at the focus of the three-lens setup.

# Chapter 7

## Conclusions and Future Work

### 7.1 Future Work

#### 7.1.1 At CU-WARG Laboratory

At the time the Centaurus laser tests were complete at low power, our laboratory was unprepared to utilize the main laser at high peak power to generate a plasma. As discussed in 6.2.1, the main laboratory laser has a post-amplification beam diameter of 30mm, which is three times larger than the beam radius for which the experiment was designed. The iris we installed to decrease the overall beam radius is not well-suited for high-power applications, necessitating a more purpose-built de-magnifying telescope.

The main laser has a high-enough intensity that the Kerr effect becomes non-negligible. The index of refraction for any transmissive material includes a nonlinear term proportional to the square of the intensity of incident light. In most applications, light is not intense enough to change the index of refraction significantly. However, in the context of our laboratory, our laser is powerful enough for pulse stretching to occur through the Kerr effect, reducing the usable peak power. We can quantify this via the *B-integral*:

$$B = \frac{2\pi}{\lambda} \int n_2 I(z) dz \quad (7.1)$$

where  $n_2$  is the nonlinear index of refraction and  $I(z)$  is the intensity of the laser with respect to its path. The magnitude of the B-integral describes the nonlinear phase shift of the laser as a result of the Kerr effect, and allows an estimation of the degree to which the pulse is stretched due, inevitably leading to a loss in laser power. Maximal laser power results from minimizing the B-integral; realistically, this is only possible by reducing the number of transmissive optics, which contribute to the B-integral's magnitude. If we were to use two fused-silica lenses of thickness  $\approx 3\text{mm}$  each, with a nonlinear index of refraction of  $\approx 2.5 \times 10^{-20} \frac{\text{W}}{\text{m}^2}$  [42], we can evaluate the B-integral for our laser. We will use the parameters for the CU-WARG Centaurus laser at maximum output, and assume that the pulse energy

of 500 mJ is evenly-distributed across the initial 30cm pulse.

$$B = \frac{2\pi}{800 \text{ nm}} \left[ \int_0^{0.003} n_2 \left( 1.77 \times 10^{16} \frac{\text{W}}{\text{m}^2} \right) dz + \int_0^{0.003} n_2 \left( 1.59 \times 10^{17} \frac{\text{W}}{\text{m}^2} \right) dz \right] \quad (7.2)$$

$$= 104.167$$

Pulse stretching due to the Kerr effect becomes a problem when the B-integral is greater than one. This precludes the use of conventional lenses to reduce the beam radius.

A proposed method of sidestepping this makes use of curved mirrors in place of traditional lenses. By placing a converging mirror and a diverging mirror at a precise separation, it is possible for them to act as a beam reducer telescope in the same way as a more conventional Galilean lens combination. This would reduce the main laser to the desired beam radius without increasing the value of the B-integral.

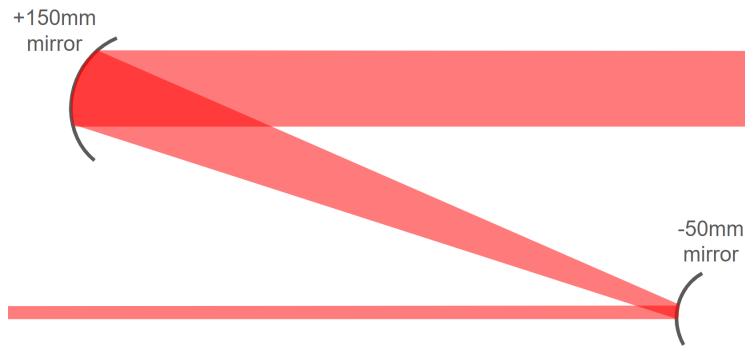


Figure 7.1: Schematic of the reflective beam-reducer telescope. Beam is incident from the right side of the figure.

This will allow plasma to be generated at the CU-WARG laboratory. The CU-WARG group has previously developed a suite of plasma analysis techniques using shadowgraphy and afterglow analysis, allowing for diagnostic of the plasma density and dimensions [43]. This will allow a range of diagnostic experiments where the laser energy, gas density, and plasma species can be varied to determine the optimal parameters for generating a plasma lens. This provides the best opportunity for fine-tuning the experimental setup for use with an accelerated electron beam.

### 7.1.2 At SLAC

The CU-WARG laboratory has no capability to generate or manipulate relativistic electron beams. After it has been shown that the cylindrical lens scheme is capable of generating a plasma of the correct size and dimension, we will replicate our setup at SLAC National Accelerator Laboratory, where we will verify the ability of the plasma lens to focus a relativistic

electron beam. SLAC uses a similar laser system to the CU-WARG Centaurus laser, with a 40 fs pulse length and a peak power of 10 TW [44], and can use a gas-jet for the plasma source instead of a static-filled vacuum chamber, if desired.

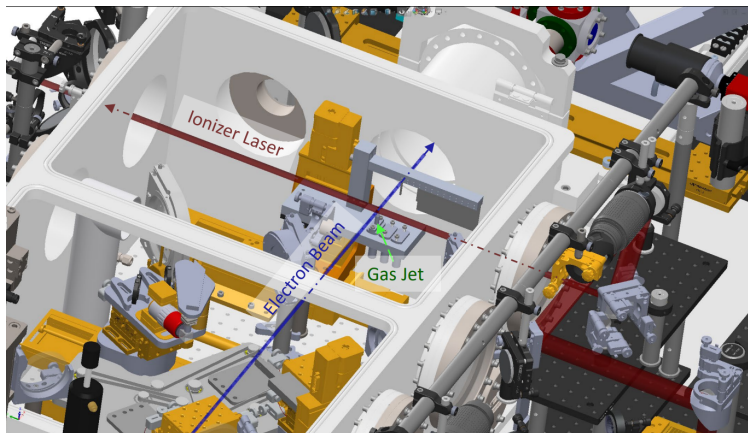


Figure 7.2: SLAC experimental vacuum chamber installed along the electron beam line. Gas from a gas jet is ionized by a laser pulse to form a plasma lens, which then focuses the relativistic electron beam. [28]

## 7.2 Conclusions

The laser-ionized plasma lens is highly-dependent on having an incident beam of the correct size. Small departures from the ideal beam diameter of 10mm can significantly increase both the Rayleigh length of the laser and the focused beam waist size. Since the plasma lens is designed to be less than a betatron wavelength for an accelerated electron in a wakefield, the increased plasma lens thickness could significantly alter the effective focal length from the target value.

The capability of this design to effectively ionize plasma still has yet to be tested. In order to fit the lens system into Experimental Chamber B, several mirrors were added downstream of the lenses in order to give the laser adequate space to propagate and to place the beam waist within the desired final region. With the main laser at low power, there was no danger of damaging any optical components. However, the significantly-higher output energy of the laser at maximum power likely makes the pulse intense enough to cause damage in this regime. In this case, the design would need to be altered to prevent this.

We have shown that the desired Gaussian beam focus, with transverse diameters of  $37.4\ \mu\text{m}$  and  $118.5\ \mu\text{m}$  respectively, can be generated using a combined system of a +200mm converging cylindrical lens in conjunction with a -100mm diverging cylindrical lens, upstream of a +700mm converging cylindrical lens rotated  $90^\circ$  relative to the other two lenses, and that they are able to do so with a high degree of precision and without overly-fine control over the placement of the lenses.

# Bibliography

- [1] Sören Möller. *Accelerator Technology: Applications in Science, Medicine, and Industry*. Springer Nature, 2020.
- [2] ATLAS Collaboration. Observation of a new particle in the search for the standard model higgs boson with the atlas detector at the lhc. *Physics Letters B*, 716(1):1–29, September 2012. ISSN 0370-2693. doi: 10.1016/j.physletb.2012.08.020.
- [3] A.Yu. Ignatiev and R.R. Volkas. Discovering mirror particles at the large hadron collider and the implied cold universe. *Physics Letters B*, 487(3–4): 294–298, August 2000. ISSN 0370-2693. doi: 10.1016/s0370-2693(00)00836-4.
- [4] ATLAS Collaboration. Observation of a new  $\chi$  b state in radiative transitions to  $\gamma$  (1 s) and  $\gamma$  (2 s) at atlas. *Physical Review Letters*, 108(15):152001, 2012.
- [5] H Albrecht, H Ehrlichmann, T Hamacher, RP Hofmann, T Kirchhoff, A Nau, S Nowak, H Schröder, HD Schulz, M Walter, et al. Observation of a new charmed baryon. *Physics Letters B*, 317(1-2):227–232, 1993.
- [6] Robert Appleby and R Aaij. Observation of excited lambda.b0 baryons. *Phys. Rev. Lett.*, 109, 2012.
- [7] R Bernet, K Müller, O Steinkamp, U Straumann, A Vollhardt, and LHCb Collaboration. Study of dj meson decays to  $d^+ \pi^-$ ,  $d^0 \pi^+$  and  $d^+ \pi^-$  final states in pp collision. *Journal of High Energy Physics*, 2013:145, 2013.
- [8] S Belforte, Vieri Candelise, M Casarsa, B Gobbo, Chiara LA LICATA, Matteo Marone, Damiana Montanino, A Penzo, Andrea Schizzi, A Zanetti, et al. Observation of a peaking structure in the  $j/\psi$  phi mass spectrum from  $b^{+/-}$  to  $j/\psi$  phi  $k^{+/-}$ -decays. *PHYSICS LETTERS. SECTION B*, 734:261–281, 2014.
- [9] Georges Aad, Brad Abbott, Jalal Abdallah, S Abdel Khalek, R Aben, B Abi, M Abolins, OS AbouZeid, H Abramowicz, H Abreu, et al. Observation of an excited  $b c \pm$  meson state with the atlas detector. *Physical review letters*, 113(21): 212004, 2014.
- [10] Ugo Amaldi. The importance of particle accelerators. *Europhysics News*, 31:5–9, 11 2000. doi: 10.1051/epn:2000601.
- [11] Oscar Barbalat. Applications of particle accelerators; rev. version, 1994.
- [12] Dace Steinberga and Normunds Stivrins. Fire frequency during the holocene in central latvia, northeastern europe. *Estonian Journal of Earth Sciences*, 70(3): 127–139, 2021.
- [13] R. C. Dhuley, I. Gonin, S. Kazakov, T. Khabiboulline, A. Sukhanov,

- V. Yakovlev, A. Saini, N. Solyak, A. Sauers, J. C. T. Thangaraj, K. Zeller, B. Coriton, and R. Kostin. Design of a 10 mev, 1000 kw average power electron-beam accelerator for wastewater treatment applications. *Phys. Rev. Accel. Beams*, 25:041601, Apr 2022. doi: 10.1103/PhysRevAccelBeams.25.041601.
- [14] B.N. Turman, R.J. Kaye, and J.A. Jacobs. An overview of electron beam decontamination technology and applications. In *Conference Record of the Twenty-Fifth International Power Modulator Symposium, 2002 and 2002 High-Voltage Workshop.*, pages 39–43, 2002. doi: 10.1109/MODSYM.2002.1189422.
- [15] Shannon L. Helfinstine, Carlos Vargas-Aburto, Roberto M. Uribe, and Christopher J. Woolverton. Inactivation of bacillus endospores in envelopes by electron beam irradiation. *Applied and Environmental Microbiology*, 71(11):7029–7032, 2005. doi: 10.1128/AEM.71.11.7029-7032.2005.
- [16] Patricia Stanfill Edens. Linear accelerator and cancer., May 2022.
- [17] Victor Etxebarria, Jorge Feuchtwanger, Joaquin Portilla, Josu Jugo, Inigo Arredondo, Inari Badillo, Estibalitz Asua, Rafael Enparantza, Iratxe Ariz, Unai Etxebeste, et al. Manufacturing of radiopharmaceutical isotopes through the linac 7 accelerator for biomedical applications. *DYNA*, 97(3):301–307, 2022.
- [18] Walter Henning. *Accelerators for america's future*. Sandbox Studio, 2010.
- [19] Helmut Wiedemann. *Particle Accelerator Physics*. Springer, August 2015.
- [20] Richard L. Taylor. Magnetic measurements of quadrupole focusing magnets at SLAC, 8 1991.
- [21] David H. McIntyre. *Quantum Mechanics: A Paradigms Approach*. Cambridge University Press, 2022.
- [22] Maxim V Ammosov, Nikolai B De-lone, and Vladimir P Krainov. Tunnel Ionization Of Complex Atoms And Atomic Ions In Electromagnetic Field. In John A. Alcock, editor, *High Intensity Laser Processes*, volume 0664, pages 138 – 141. International Society for Optics and Photonics, SPIE, 1986. doi: 10.1117/12.938695.
- [23] Ihar Shchatsinin. *Free clusters and free molecules in strong, shaped laser fields*. PhD thesis, Freie Universität Berlin, 2009.
- [24] Alexander David Cahill. Ultra-high accelerating gradients in radio-frequency cryogenic copper structures. *Ph. D. Thesis*, 2017.
- [25] Walter Wuensch. High-Gradient Breakdown in Normal-Conducting RF Cavities, 2002.
- [26] B. Woolley, G. Burt, A. C. Dexter, R. Peacock, W. L. Millar, N. Catalan Lasheras, A. Degiovanni, A. Grudiev, G. Mcmonagle, I. Syratchev, W. Wuensch, E. Rodriguez Castro, and J. Giner Navarro. High-gradient behavior of a dipole-mode rf structure. *Phys. Rev. Accel. Beams*, 23:122002, Dec 2020. doi: 10.1103/PhysRevAccelBeams.23.122002.
- [27] T. Tajima and J. M. Dawson. Laser electron accelerator. *Phys. Rev. Lett.*, 43:

- 267–270, Jul 1979. doi: 10.1103/PhysRevLett.43.267.
- [28] Christopher E Doss. *Laser-Ionized Underdense Passive Plasma Lens for Focusing Electron Beams*. PhD thesis, University of Colorado at Boulder, 2023.
- [29] D. Gordon, K. C. Tzeng, C. E. Clayton, A. E. Dangor, V. Malka, K. A. Marsh, A. Modena, W. B. Mori, P. Muggli, Z. Najmudin, D. Neely, C. Danson, and C. Joshi. Observation of electron energies beyond the linear dephasing limit from a laser-excited relativistic plasma wave. *Phys. Rev. Lett.*, 80:2133–2136, Mar 1998. doi: 10.1103/PhysRevLett.80.2133.
- [30] None None. Technical design report for the facet-ii project at slac national accelerator laboratory, 8 2016.
- [31] C.A. Lindstrøm and M. Thévenet. Emission preservation in advanced accelerators. *Journal of Instrumentation*, 17(05):P05016, may 2022. doi: 10.1088/1748-0221/17/05/P05016.
- [32] R. Ariniello, C. E. Doss, K. Hunt-Stone, J. R. Cary, and M. D. Litos. Transverse beam dynamics in a plasma density ramp. *Phys. Rev. Accel. Beams*, 22:041304, Apr 2019. doi: 10.1103/PhysRevAccelBeams.22.041304.
- [33] R. Ariniello, C. E. Doss, V. Lee, C. Hansel, J. R. Cary, and M. D. Litos. Chromatic transverse dynamics in a nonlinear plasma accelerator. *Phys. Rev. Res.*, 4:043120, Nov 2022. doi: 10.1103/PhysRevResearch.4.043120.
- [34] S. A. Yi, V. Khudik, C. Siemon, and G. Shvets. Analytic model of electromagnetic fields around a plasma bubble in the blow-out regime. *Physics of Plasmas*, 20(1):013108, 01 2013. ISSN 1070-664X. doi: 10.1063/1.4775774.
- [35] T. N. Dalichaouch, X. L. Xu, A. Tableman, F. Li, F. S. Tsung, and W. B. Mori. A multi-sheath model for highly nonlinear plasma wakefields. *Physics of Plasmas*, 28(6):063103, 06 2021. ISSN 1070-664X. doi: 10.1063/5.0051282.
- [36] C. E. Doss, E. Adli, R. Ariniello, J. Cary, S. Corde, B. Hidding, M. J. Hogan, K. Hunt-Stone, C. Joshi, K. A. Marsh, J. B. Rosenzweig, N. Vafaei-Najafabadi, V. Yakimenko, and M. Litos. Laser-ionized, beam-driven, underdense, passive thin plasma lens. *Phys. Rev. Accel. Beams*, 22:111001, Nov 2019. doi: 10.1103/PhysRevAccelBeams.22.111001.
- [37] *Mai Tai Ultrafast One Box Ti:Sapphire Lasers*. Spectra-Physics, 2021.
- [38] R. Paschotta. Chirp. RP Photonics Encyclopedia, Nov 2007.
- [39] E. Hecht. *Optics*. Pearson Education, Incorporated, 2017. ISBN 9780133977226.
- [40] R. Paschotta. Gaussian beams. RP Photonics Encyclopedia, May 2005.
- [41] I. H. Malitson. Interspecimen comparison of the refractive index of fused silica\*,†. *J. Opt. Soc. Am.*, 55(10):1205–1209, Oct 1965. doi: 10.1364/JOSA.55.001205.
- [42] Robert Adair, L. L. Chase, and Stephen A. Payne. Nonlinear refractive index of optical crystals. *Phys.*

- Rev. B*, 39:3337–3350, Feb 1989. doi: 10.1103/PhysRevB.39.3337.
- [43] Valentina Lee, Robert Ariniello, Christopher Doss, Keenan Hunt-Stone, Kathryn Wolfinger, and Michael Litos. PWFAs Plasma Source Density and Width Measurement by Robust Optical Methods. In *APS Division of Plasma Physics Meeting Abstracts*, volume 2021 of *APS Meeting Abstracts*, page UO05.011, January 2021.
- [44] S. Z. Green, E. Adli, C. I. Clarke, S. Corde, S. A. Edstrom, A. S. Fisher, J. Frederico, J. C. Frisch, S. Gessner, S. Gilevich, P. Hering, M. J. Hogan, R. K. Jobe, M. Litos, J. E. May, D. R. Walz, V. Yakimenko, C. E. Clayton, C. Joshi, K. A. Marsh, N. Vafaei-Najafabadi, and P. Muggli. Laser ionized preformed plasma at FACET. *Plasma Physics and Controlled Fusion*, 56(8):084011, August 2014. doi: 10.1088/0741-3335/56/8/084011.